Refractive interstellar scintillation in pulsar dynamic spectra

Yashwant Gupta,[1] Barney J. Rickett[2] and Andrew G. Lyne[3]

[1] *National Centre for Radio Astrophysics, TIFR, Post Bag 3, Ganeshkhind, Pune 411 007, India*
[2] *Department of Electrical and Computer Engineering, University of California, San Diego, CA 92093-0407, USA*
[3] *University of Manchester, Nuffield Radio Astronomy Laboratories, Jodrell Bank, Macclesfield SK11 9DL*

ABSTRACT

The evolution of the dynamic spectra of eight pulsars over 16 months is reported. Observations were made at Jodrell Bank at 408 MHz from 1984 September to 1986 January. The changing form of the spectra is interpreted as refractive modulation of diffractive interstellar scintillation. The correlation function versus time and frequency was computed for each observation and estimates were made of the apparent decorrelation widths in frequency and time, and the frequency drift rate of scintillation features.

A model is developed for how these three parameters vary with epoch under changing angles of refraction. The model successfully describes the variations for four of the pulsars, for which the drift rate shows some sign reversals between epochs. Two pulsars kept a constant sign of drift rate, which we interpret as due to persistent refracting structures in their lines of sight, which are consistent with an intervening H II region. Studies were made of the variability of the diffractive bandwidth, the visibility of the drifting features in the dynamic spectra, the refractive shifts and the speed estimated for the diffraction pattern. The pulsar PSRB2016+28, which has an unusually low proper motion, shows clear modulation of the pattern speed by the Earth's annual motion.

In the 11 epochs observed for PSRB2016+28, two showed unmistakable periodic modulation in the dynamic spectra. Several other pulsars exhibited occasional periodic patterns with low modulation. The phenomenon varies substantially between the pulsars, being more common for lower strengths of scattering.

Key words: radiative transfer – pulsars: general – pulsars: individual: PSRB2016+28 – ISM: general.

1 INTRODUCTION

The modulation seen in the dynamic spectra of pulsar intensities, when averaged over many pulses, was the first observational clue to the existence of random variations in the plasma density of the interstellar medium (ISM) (Scheuer 1968; Rickett 1969). Observations of pulsar dynamic spectra have since proved to be a rich source of information on the irregular ISM (e.g. Cordes, Weisberg & Boriakoff 1985; Cordes 1986). The basic interpretation is that the random density variations along the interstellar propagation path strongly modulate the phase of the waves, creating an angular spectrum of waves, which interfere with each other as they propagate and so cause a diffraction pattern with amplitude variations. An observer sees the amplitude varying with time, due to relative motion of the Earth through the diffraction pattern; the motion involves an effective velocity that depends on the velocities of the Earth, the pulsar and the density irregularities. There are large-amplitude fluctuations which have characteristic scales

in space (and so time) and in observing frequency, termed diffractive interstellar scintillation (DISS).

Observers have also noted apparently systematic effects in the dynamic spectra, in addition to the random DISS modulations. Ewing et al. (1970), Roberts & Ables (1982), Hewish, Wolszczan & Graham (1985) and Cordes, Pidwerbetsky & Lovelace (1986) observed systematic drifts of intensity maxima in frequency versus time. Smith & Wright (1985) reported the slopes of the frequency drifts for a number of pulsars, observed at a single epoch. In addition, observers have also noted occasional periodic intensity modulations in frequency and/or time (e.g. Wolszczan & Cordes 1987), which they have explained as interference of waves coming from two or three discrete directions of arrival.

Under strong scintillation, which applies for typical radio astronomical observing frequencies and distances, the diffractive scintillation pattern can itself be modulated by random refractive effects (see Prokhorov et al. 1975 for a review of wave propagation theory). Such refractive interstellar scintilla-

1036   *Y. Gupta, B. J. Rickett and A. G. Lyne*

Table 1. Predicted time-scales and observational details.

Pulsar	DM (pc cm^{-3})	Z (kpc)	τ_d (sec)	τ_r (days)	1st day 09-84	δt (sec)	No. obs.
P0329+54	26.8	2.30	190	7.5	9	28	10
P0628-28	34.4	1.30	350	9.5	18	28	9
P0823+26	19.5	0.71	225	2.4	8	28	11
P0834+06	12.9	0.43	171	8.8	8	28	14
P1133+16	4.8	0.15	100	0.44	9	28	10
P1642-03a	35.7	1.3	59	4.6	7	28	11
P1642-03b	35.7	0.15	59	13.1	7	28	11
P1929+10	3.176	0.11	460	1.9	7	28	13
P2016+28	14.2	1.3	606	68	8	58	11

tions (RISS) have been recognized in the long-term variations of pulsars (Rickett, Coles & Bourgois 1984) and of other radio sources (e.g. Dennison et al. 1984; Rickett 1986). Refractive effects have also been proposed as the basic cause of the 'systematic' variations in pulsar dynamic spectra. Theoretical analyses of refractive interstellar effects have been made by Cordes et al. (1986) and by Romani, Narayan & Blandford (1986). They give expected values for the slopes of features drifting in frequency and time, based on power-law models of the interstellar wavenumber spectrum for electron density. In such studies a diffractive angle θ_d and a refractive angle θ_r are defined. Roughly speaking, diffraction by small-scale irregularities broadens the instantaneous angular spectrum into a cone of radius θ_d, while refraction by larger scale irregularities in the ISM displaces the centroid of this spectrum by an angle θ_r that varies slowly with frequency and time. Differing forms of the density spectrum lead to differing predictions about the ratio of θ_r to θ_d, about how θ_r varies spatially and about any substructure to the scattered image. Whereas a power-law spectrum of the Kolmogorov form would explain most of the frequency drifts with $\theta_r < \theta_d$, a steeper power law that gives $\theta_r > \theta_d$ seems to be needed to explain the periodic fringe phenomena sometimes seen. Spangler (1988) has emphasized the inconsistency of these viewpoints. Goodman et al. (1987) have analysed the influence of caustics in the propagation process, particularly generated by a wavenumber spectrum that is a power-law form cut off by a high-wavenumber 'dissipation'. Dissipation here refers to the idea that a Kolmogorov spectrum caused by a turbulent cascade over many decades in wavenumber may be terminated by dissipation at a characteristic (small) scale; there is, however, a parallel possibility of a reverse cascade from small to large scales. The occasional influence of caustics is a promising explanation of the inconsistent conclusions about θ_r and θ_d (Goodman et al. 1987).

The observations reported in the present paper were planned to study the temporal evolution and distance dependence of systematic effects in pulsar dynamic spectra, with a view to an improved understanding of the phenomena discussed above and of the interstellar density spectrum.

2 OBSERVATIONS OF DYNAMIC SPECTRA

2.1 Observing parameters

The observations were made using the 76-m Lovell telescope at Jodrell Bank, England. Observations were made at a centre frequency of 408 MHz for 8 pulsars at $12 - 14$ epochs spanning 16 months from 1984 September to 1986 January. Dynamic spectra of the sum of two circular polarizations were recorded over a 5-MHz bandwidth for durations ranging from 1 to 4 h. There were 256 spectral estimates across the band, derived from an auto-correlation spectrometer giving a spectral resolution of about 20 kHz. The auto-correlator was gated in synchronism with the pulsar period, for an 'on-pulse' window and an 'off-pulse' window. Data were averaged for 30 to 60 s and recorded together with total power estimates. These allowed proper power normalization for the on and off pulse spectra, which were then subtracted to obtain estimates of the pulsar spectrum itself. A standard radio source was observed at each epoch to convert the power calibration to jansky: the dispersion measure

and assumed distance are taken from Cordes (1986); from the same reference we list the diffractive scintillation time scaled to 408 MHz (τ_d) and the predicted refractive scintillation time at 408 MHz (τ_r). The latter is calculated using equation (3a) of Gupta, Rickett & Coles (1993) with the diffractive decorrelation bandwidth from Cordes (1986) and the proper motion velocity from Lyne, Anderson & Salter (1982). Parameters of the observations are also given in columns 6-8 of Table 1: for each source the date of the first observation, the time resolution for the dynamic spectra and the number of epochs observed. The dynamic spectra were recorded over periods substantially longer than τ_d, which in turn is longer than the time resolution. An exception was PSRB1133+16 for which the time resolution was comparable to a fine time-scale observed in the spectra; PSRB1642-03 exhibited a longer time-scale than the predicted value of 59 s and was adequately resolved. The predicted refractive time-scale for most of the pulsars was shorter than the typical interval between epochs, which ranged from 1 to 190 d. Thus the refractive variations are substantially undersampled in these observations.

Samples of the dynamic spectra are shown in Figs 1(a)-(h). In each figure a single panel shows the dynamic spectra as a grey scale over 4.5 MHz for durations ranging from 1 to 2.5 h. The display saturates at black for intensities above 75 per cent of the maximum and at white below 6 per cent of the maximum; in between, the intensity is linearly represented by the density. There are islands of increased intensity distributed randomly over the frequency-time display; these are the peaks of diffractive scintillation, which we will refer to as 'scintles'. The occasional horizontal dark and light bands in the dynamic spectra are due to bursts of broadband interference. The different panels present observations on the day numbers indicated (relative to the first day of each sequence, as given in column 6 of Table 1). In Figs 1(a)-(c) sets of 9 panels are shown for pulsars PSRB0329+54, PSRB0823+26 and PSRB2016+28, extending over 480 d. In Figs 1(d)-(h) sets of 3 panels are shown for the remaining pulsars. The 3 panels are chosen to represent typical dynamic spectra, to illustrate the differences between the pulsars. The observing schedule was chosen to give observations at intervals ranging from 1 to 190 d and also to span 16 months, subject to other telescope scheduling constraints. Our expectation was that the slopes and widths of the diffractive scintles will change over the same characteristic time as for RISS intensity variations. As discussed in Section 3, variations in the slope and frequency
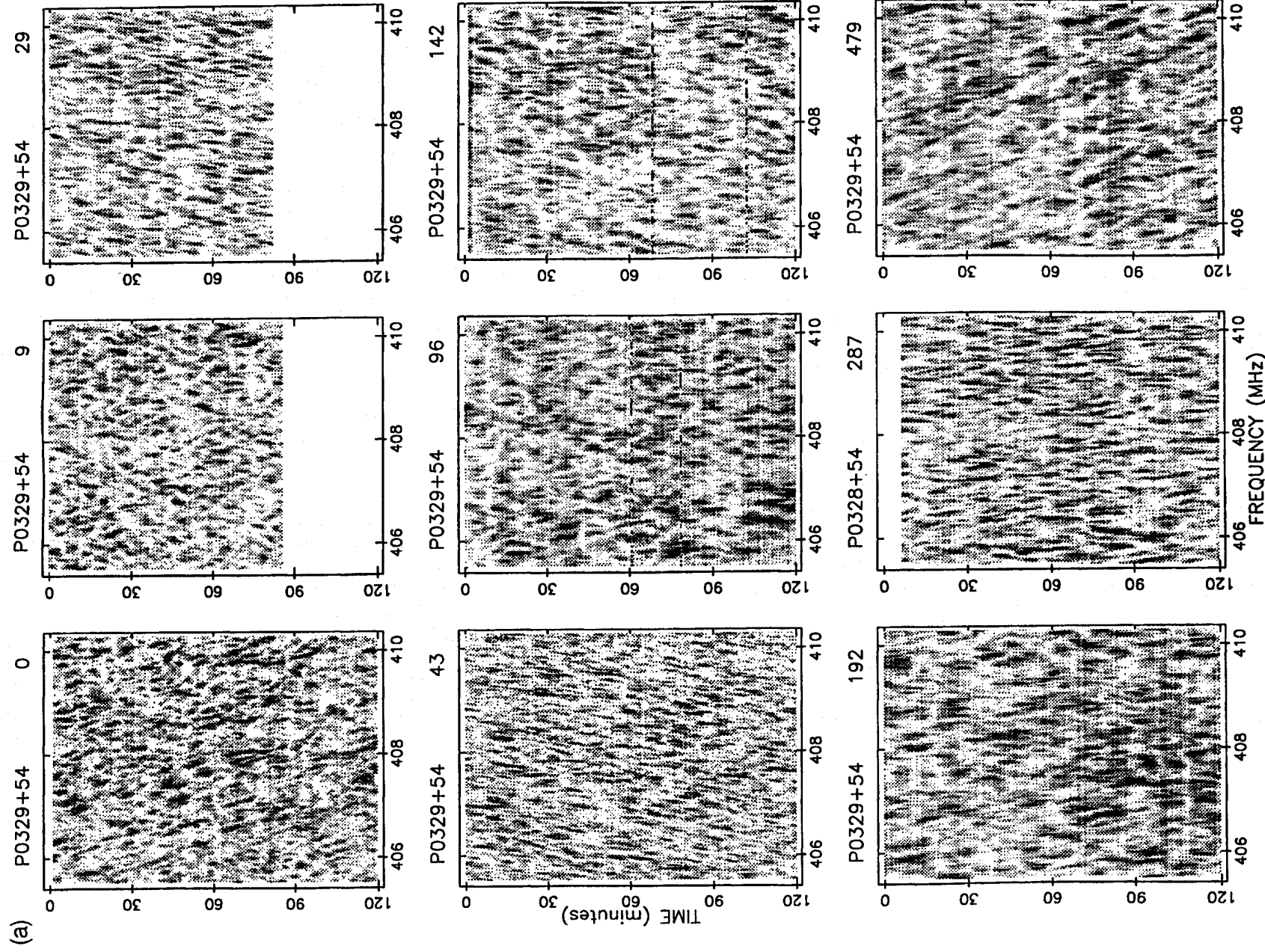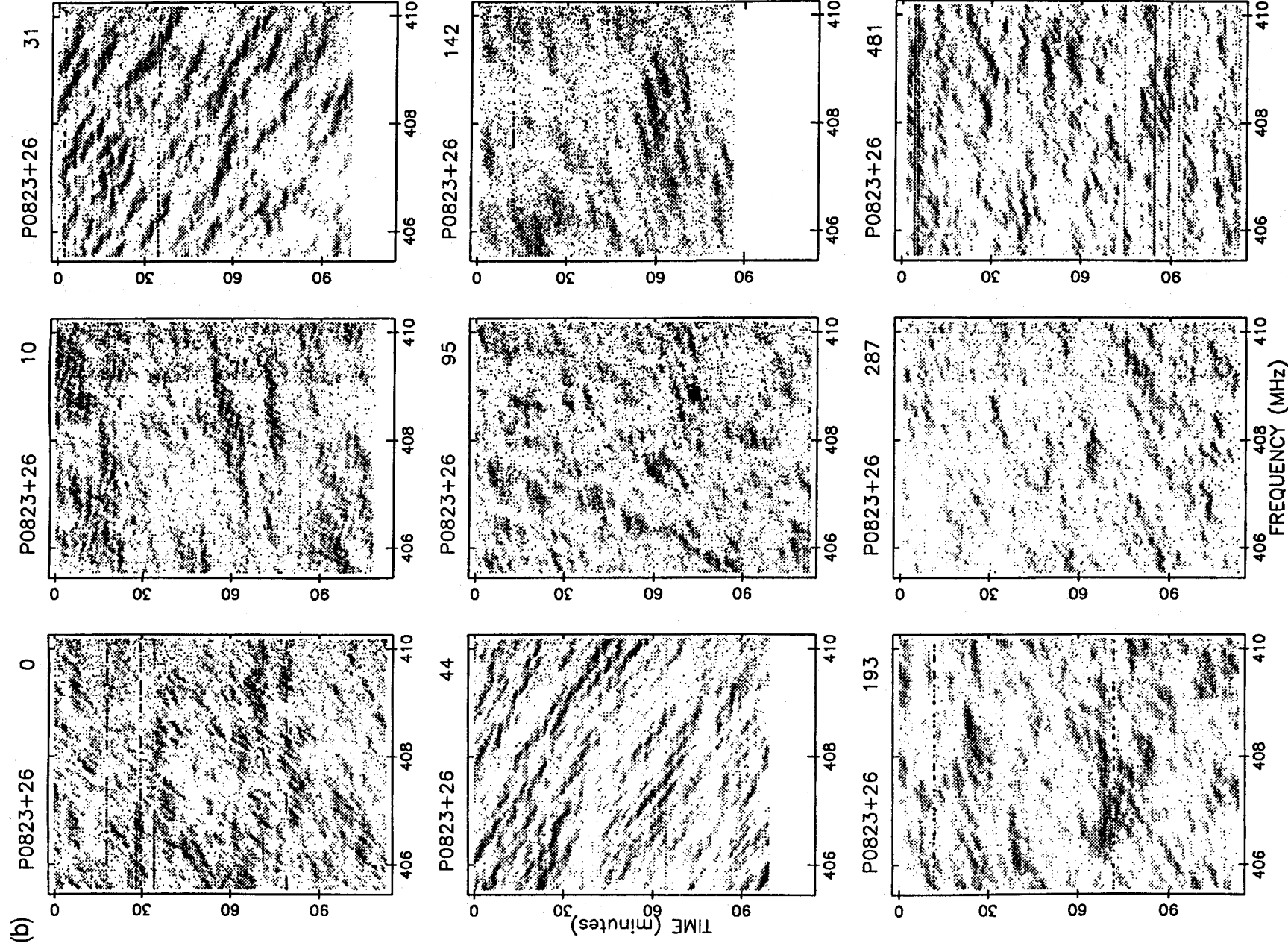
Figure 1. The dynamic spectra of the pulsars plotted as a grey scale plot of intensity versus time and frequency for (a) PSRB0329+54; (b) PSRB0823+26; (c) PSRB2016+28. Darker pixels correspond to higher intensity values; the density is a linear representation of density, saturating at black at 90 per cent of the maximum and saturating at white at 5 per cent of the maximum. Data for 9 epochs are shown, with the day number given relative to 1984 September 9. The frequency resolution is 19.5 kHz; the time resolution is 28 s (except for PSRB1929+10 and PSRB2016+28 where it is 58 s). (d)–(h) Typical dynamic spectra plotted for three sample epochs: (d) PSRB0628-28; (e) PSRB0834+06; (f) PSRB1133+16; (g) PSRB1642-03; (h) PSRB1929+10. The reference dates for each pulsar are given in Table 1.
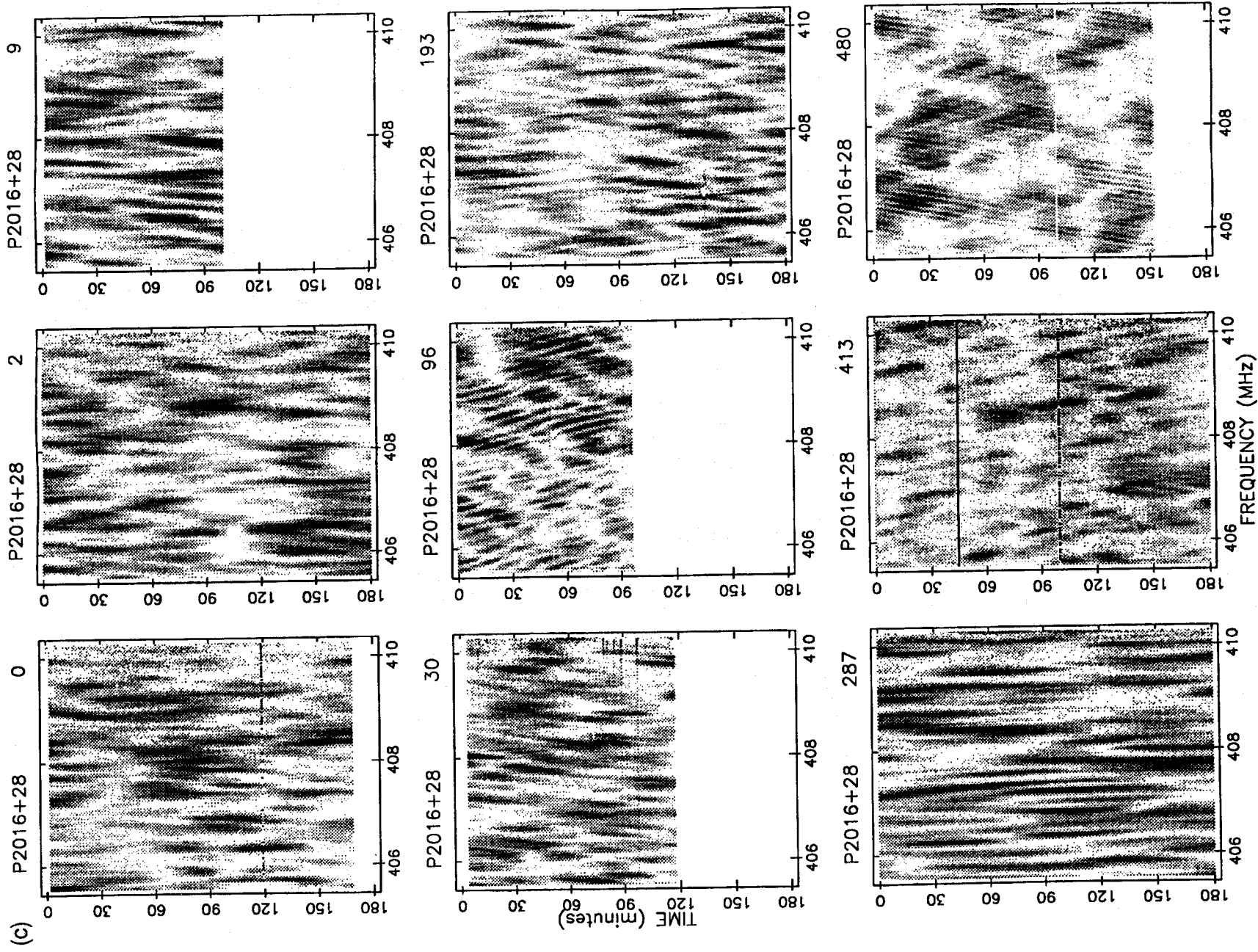
© Royal Astronomical Society • Provided by the NASA Astrophysics Data System

(b)

Figure 1 – *continued*

FREQUENCY (MHz)

TIME (minutes)

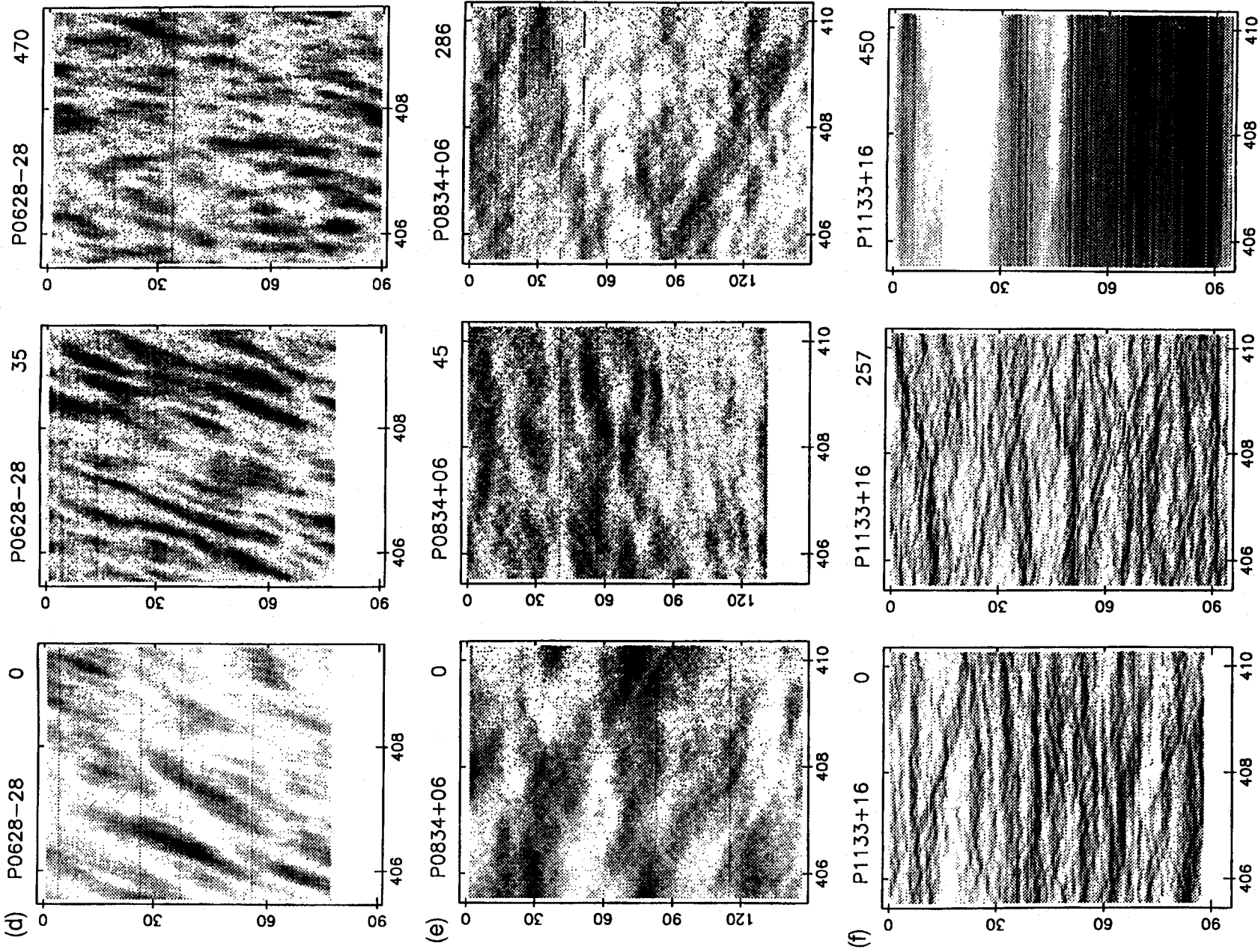Figure 1 – *continued*

FREQUENCY (MHz)

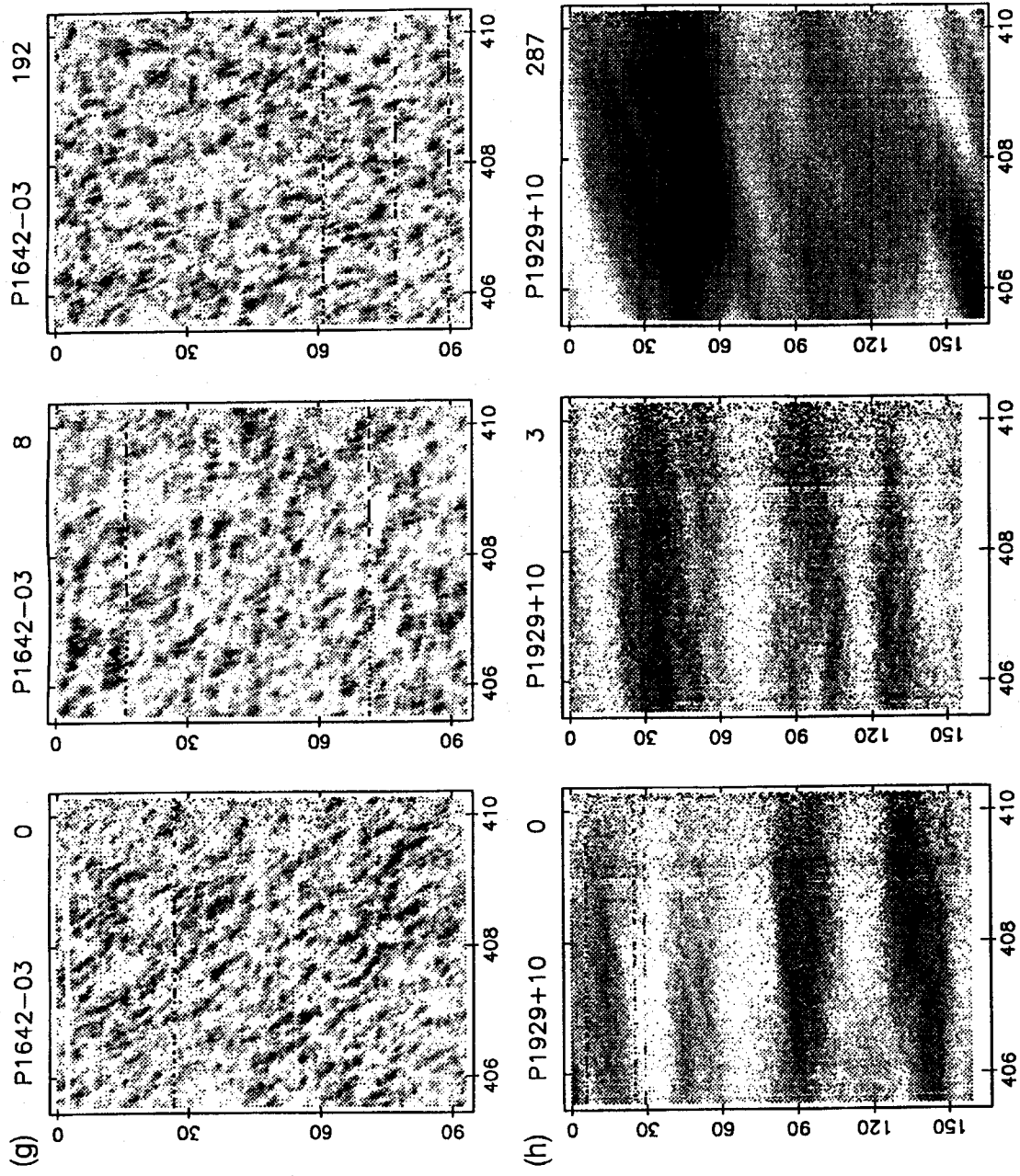TIME (minutes)

Figure 1 – continued

Figure 1 – *continued*

width are expected to be partially correlated with RISS intensity variations (averaged over many diffractive scintles).

We now give a qualitative description of the data. For PSRB0329+54, the spectra are well resolved and the scintles are randomly distributed in time and frequency. One can discern persistent drifts in frequency-time, which are approximately constant over the duration of one observation, but vary between panels. PSRB0823+26 exhibits much more pronounced frequency drifting and change of slope with epoch, with two opposing slopes evident on day 10, which epoch also shows some criss-cross 'fringes'. For PSRB2016+28 the observations span many scintles in frequency but fewer in time. The characteristic scale along the time axis is noticeably different between the panels. Days 96 and 480 show pronounced fringe patterns, which persist over the full display.

For PSRB0628-28 the observations span fewer scintles; pronounced slopes persisted with the same sign over the entire 480 d. For PSRB0834+06 the characteristic frequency scale is markedly different between panels, with extreme examples displayed. There are often low-contrast periodic patterns dis-

cernible within a large scintle, giving a fine grain to the structure in frequency and time. The patterns are reminiscent of clouds in the Earth's atmosphere. Fine-scale patterns are often evident in PSRB1133+16 data, though with noticeably lower contrast on day 36. A data-taking problem for this pulsar caused the occasional horizontal lines, which invalidated the quantitative analysis of this object. PSRB1642-03 showed the most stable spectra, with a persistent slope of the same sign for all 12 epochs of observation. PSRB1929+10 has scintles wider than our 5-MHz band and modest slopes that were often like that for day 3. On day 0 this pulsar showed a periodic modulation in time that covered four cycles.

3 ANALYSIS AND MODEL FITTING

3.1 Auto-correlations

In order to characterize the slopes and the scales in frequency and in time, we computed the auto-correlation function (acf)

1042   *Y. Gupta, B. J. Rickett and A. G. Lyne*

versus frequency and time of the spectra from each epoch. The normalized acf $C(v,\tau)$ was calculated as

$$C(v,\tau) = \frac{R(v,\tau)}{R(0,0)}, \qquad (1)$$

where $R(v,\tau) = <\Delta I(f,t)\,\Delta I(f+v, t+\tau)>$. Here $\Delta I(f,t)$ is the deviation of the intensity from the mean intensity $<I>$, where $<>$ denotes an average over the range in frequency and time in observations from a single epoch. The unnormalized covariances $R(v,\tau)$ typically had a spike at zero lag in v and τ due to additive white noise. This was removed by replacing the zero lag value by an average of R at lags of ± 1 sample in time and ± 1 sample in frequency. This scheme removes the noise contribution to $R(0,0)$ – the total variance – but also reduces the apparent variance of any true pulse variation that decorrelates over 1 min in time or 20 kHz in frequency.

Fig. 2 shows the set of acfs for five pulsars. The characteristic scales in time and frequency are given by the width at a correlation level of 1/e along the time and frequency axes. The sloping features in the dynamic spectra appear as contours elongated diagonally in the correlation plots. In Fig. 2(b) PSRB0823+26 clearly shows such features which often change shape and sign between epochs. Notice that the dates are not equally spaced. The general features highlighted in the qualitative description are also evident in the correlation plots, ally evident in some panels of Fig. 1. In order to quantify further the changing form of the spectra, we fitted a simple Gaussian model to each acf, as described below.

3.2 Model acfs and time series of parameters

A simple Gaussian model for the autocorrelations was fitted to each data set in order to characterize the widths in frequency and time and the time-frequency slopes. This model was given by

$$C_g(v,\tau) = c_0 \exp[-(c_1 v^2 + c_2 v\tau + c_3 \tau^2)]. \qquad (2)$$

The correlation estimates at large lags were sometimes biased above or below zero, due to linear changes in intensity over the observing period. In such cases a 'large lag' region of $v-\tau$ was defined from visual inspection of the acf and an average over this region was subtracted from $C(v,\tau)$ before the model was fitted. This explains the presence of the parameter c_0 which was always within 5 per cent of 1.0. The fitting procedure was a search on a grid in the non-linear parameters c_1, c_2, and c_3 for the least-squared error between model and data over the central region of each acf. The search ranges were centred on initial estimates based on the 1/e crossing points along the v and τ axes. At each point a linear least-squares fit estimate was made for c_0. A coarse grid search was followed by a finer search around the optimum parameters, at a resolution of 4 per cent of the initial width estimates.

The above analysis resulted in a time series of parameters c_1, c_2, and c_3. These are shown in Figs 3(a)-(f) in the first 3 panels of the left hand column of plots. Also shown in the bottom panel in the left hand column is the mean squared error for the fit. The fourth panel in the left hand column shows the pulse intensity averaged over each observing interval, and the scintillation index is shown in the bottom panel of the right hand column of plots. Note that the observed scintillation indices are always ≈ 1 (within ± 10 per cent), in agreement with the strong scintillation assumption for diffractive fluctuations. Results are given for the six pulsars for which the model fits were reasonably successful, indicated by a mean squared error of less than about 0.05. Occasionally there are notable increases in the fitting error (e.g. day 100 for PSRB2016+28) for which the parameters may not be too meaningful. Data for PSRB1133+16 were corrupted and so were excluded from this analysis. We also excluded PSRB1929+10, since the Gaussian fit was not satisfactory; the reason is that 5 MHz was insufficient to resolve the decorrelation in frequency, which from Cordes (1986) was expected to be at 2.7 MHz.

General features of the data are as follows. For PSRB0329+54, PSRB0823+26, PSRB0834+06 and PSRB2016+28 there are clear sign-changes in c_2, which characterizes the frequency drift, often accompanied by changes over similar time-scales in c_1, which characterizes the frequency scale. For PSRB2016+28 there are also substantial changes in c_3, which characterizes the time-scale. It should be noted that the variations are for the most part undersampled, since there are often substantial changes even over intervals as short as 1 week. However, the single pair of observations on successive days shows substantial correlation for most objects. The expected times for RISS for the pulsars are given in Table 1; the expected RISS time-scales for the 4 pulsars are not inconsistent with the variations, but consistency cannot be tested due to the under-sampling. In contrast with other pulsars, PSRB0628-28 and PSRB1642-03 show no reversals in the sign of c_2 for intervals over 480 d, though there are significant variations in its magnitude and in the other parameters, on time-scales compatible with the expected RISS time. We now discuss the theoretical aspects of the wave propagation relevant to these observations.

4 THEORETICAL MODELS FOR RISS EFFECTS

4.1 Introduction

There is a central theoretical difficulty in the interpretation of RISS effects in dynamic spectra. We typically make an observation that includes many diffractive scintles in time and/or frequency but covers a time much shorter than the refractive time-scale. As a result our estimates cannot be regarded as ensemble averages of the scintillation phenomena, whereas it is ensemble average quantities that are readily predicted theoretically. The large ratio of spatial scales for refractive and diffractive changes, however, also opens up an approximation method, in which averaging over many diffractive variations gives no smoothing of the refractive variations. There are two papers that discuss a wide variety of refractive effects in strong scintillation: Cordes et al. (1986) and Romani et al. (1986). These use somewhat different approximations, but essentially rely on ray techniques to describe the refractive effects, combined with wave techniques for the diffractive effects.

As in these two papers, we use an equivalent phase screen to represent the distributed scattering irregularities. Waves passing through such a screen are scattered into an instantaneous angular spectrum. The typical angular extent θ_d can be given in terms of the field coherence scale s_0, which is the lateral scale at the phase screen over which there is a 1-rad rms phase difference. This in turn is defined in terms of D_ϕ, the structure function of geometric phase ϕ, and leads to the following definition of θ_d for radio wavenumber k:
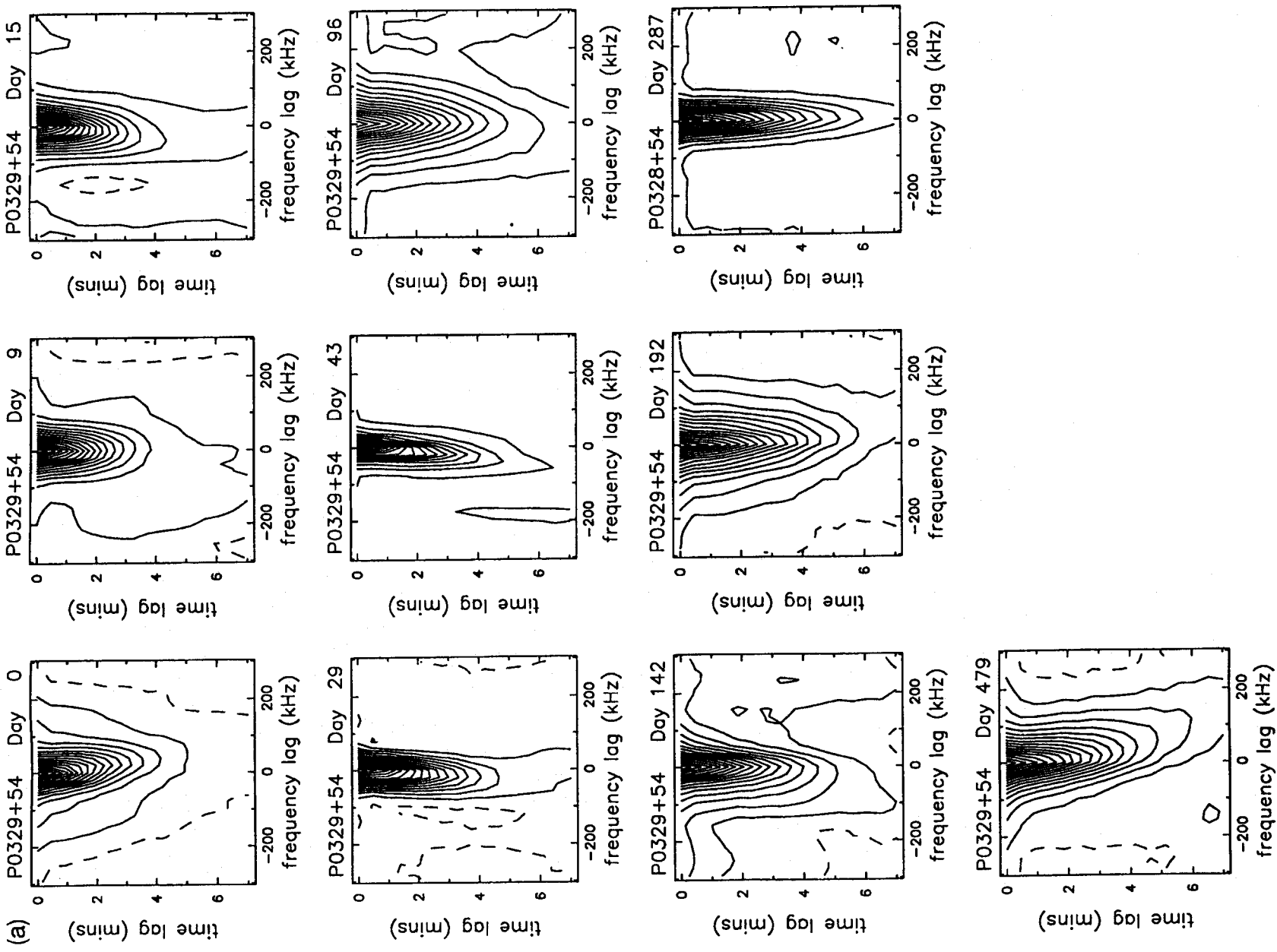
Figure 2. Two-dimensional autocorrelation functions of the dynamic spectra data for each epoch of observation, samples of which are plotted in Fig. 1. The time lag is in units of the integration time (28 s) and the frequency lag is in units of the frequency bin width (19.5 kHz). The total number of contours is 20 and the contour interval is 0.06. (a) PSRB0329+54; (b) PSRB0823+26; (c) PSRB0834+06; (d) PSRB1642−03; (e) PSRB2016+28.
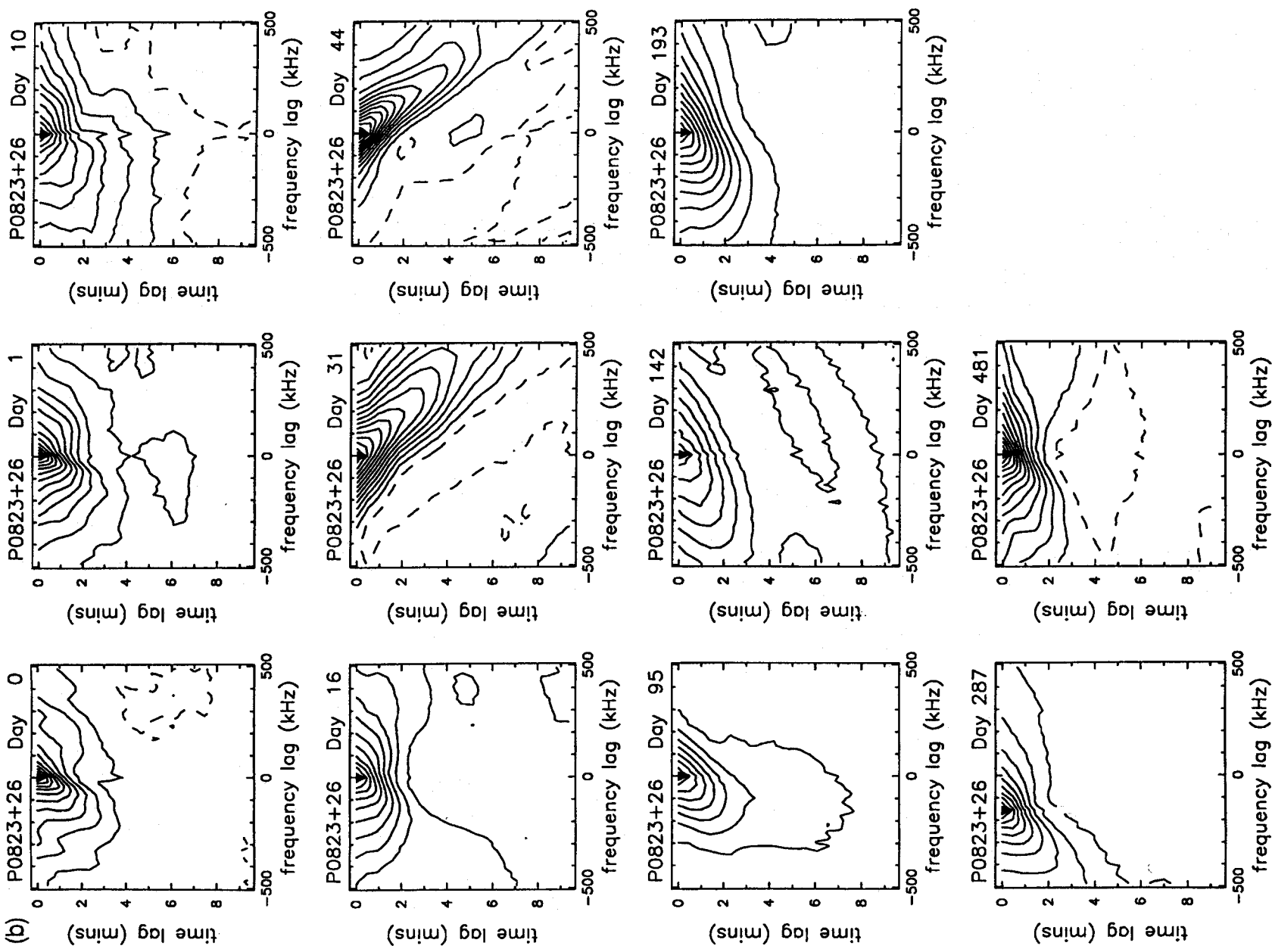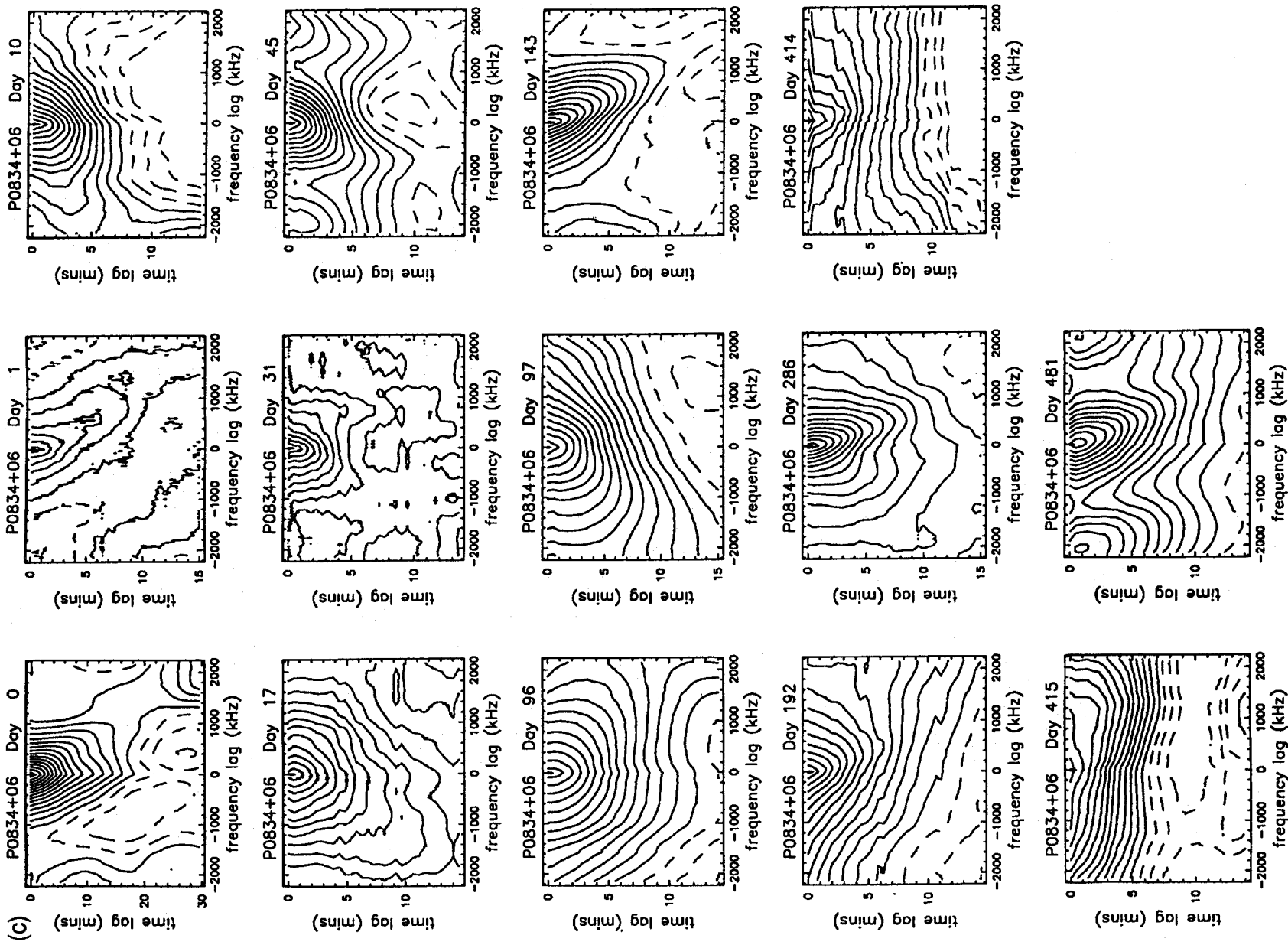
© Royal Astronomical Society • Provided by the NASA Astrophysics Data System
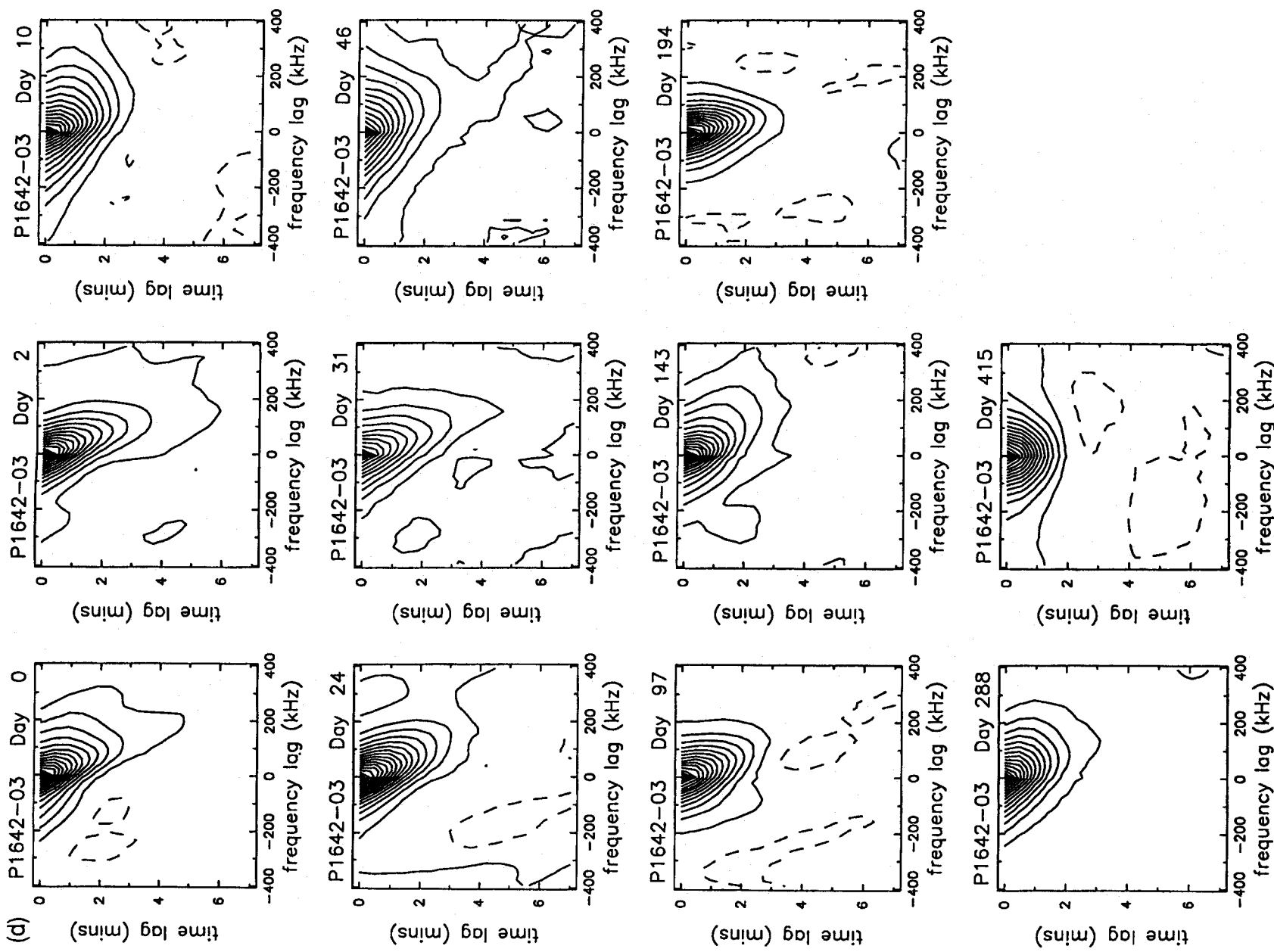
Figure 2 – *continued*

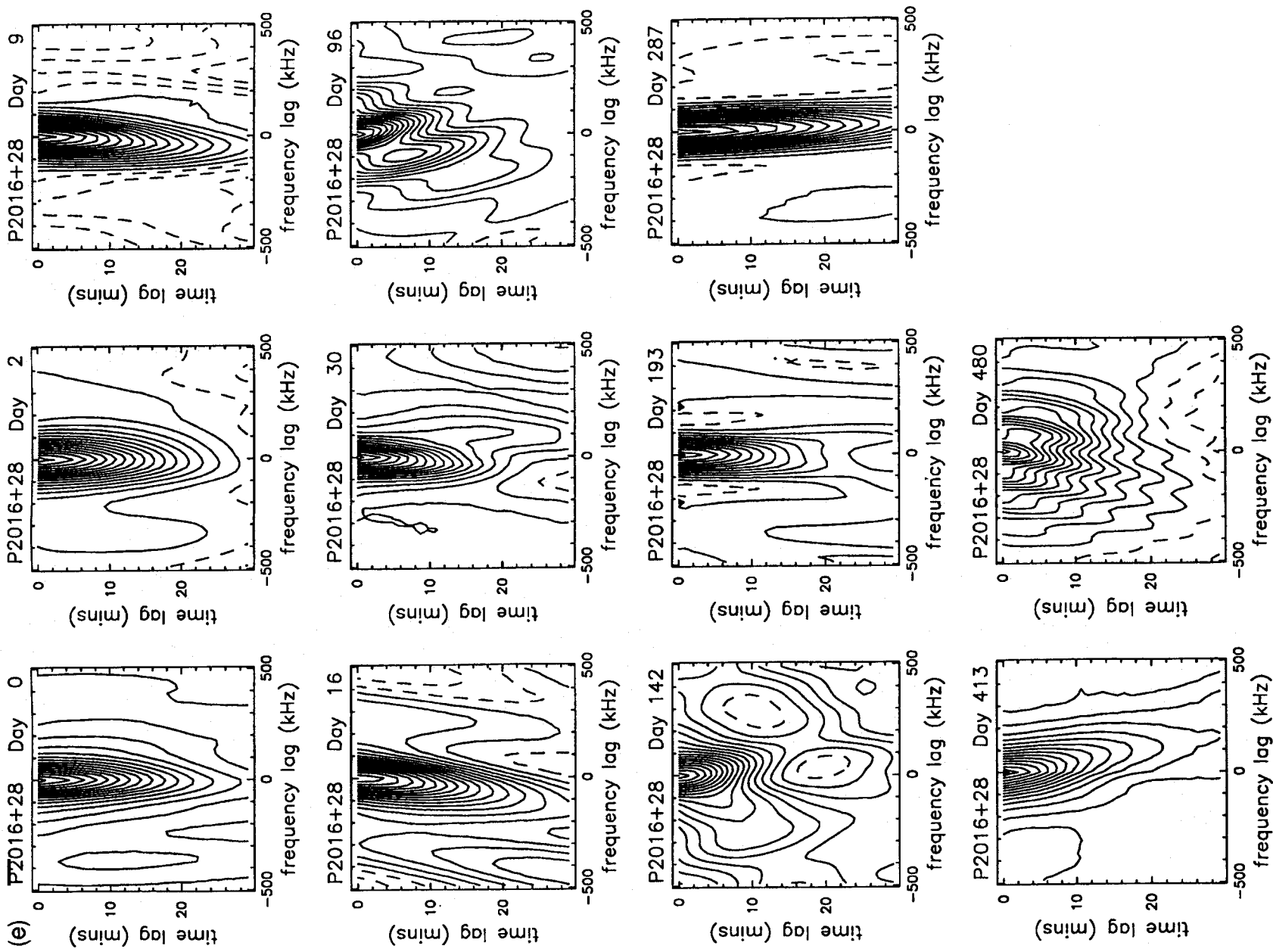Figure 2 – *continued*

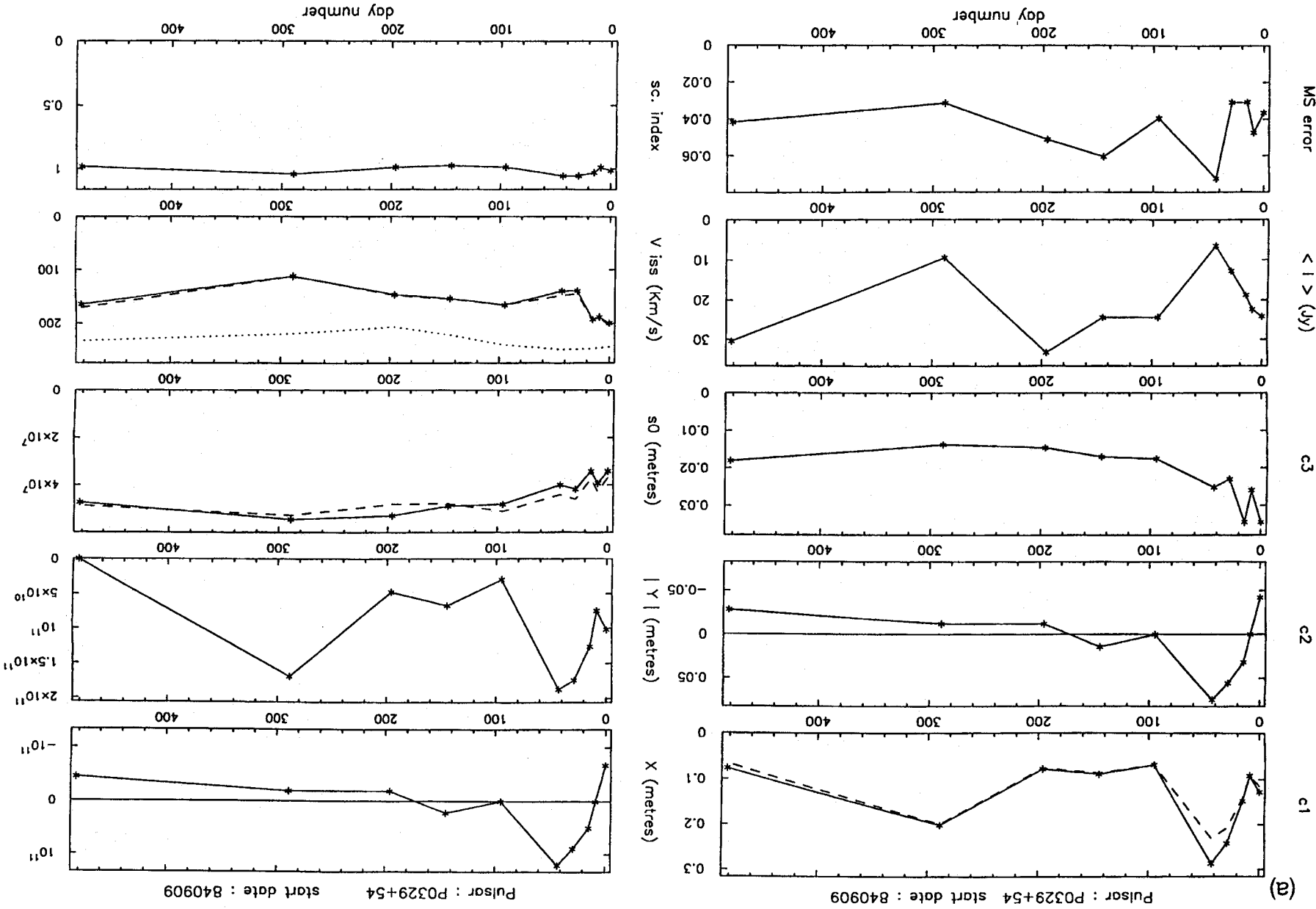Figure 2 – *continued*

Figure 2 – *continued*

Figure 3. Fitted parameters from the autocorrelation data in Fig. 2 and derived quantities versus day number. Left panels: c_1 with $c_1.\gamma$ (dashed); c_2; c_3; average intensity; mean square error for fit. Right panels: calculated refractive day shifts X and $|Y|$; coherence scale (s_0); scintillation speed V_{ISS} and scintillation index. The units for the c-parameters correspond to the time and frequency lags, 19.5 KHz and 28 s (except for PSRB2016+28 where it is 58 s). (a) PSRB0329+54; (b)PSRB0628-28; (c) PSRB0823+26; (d) PSRB0834+06; (e) PSRB1642-03; (f) PSRB2016+28.
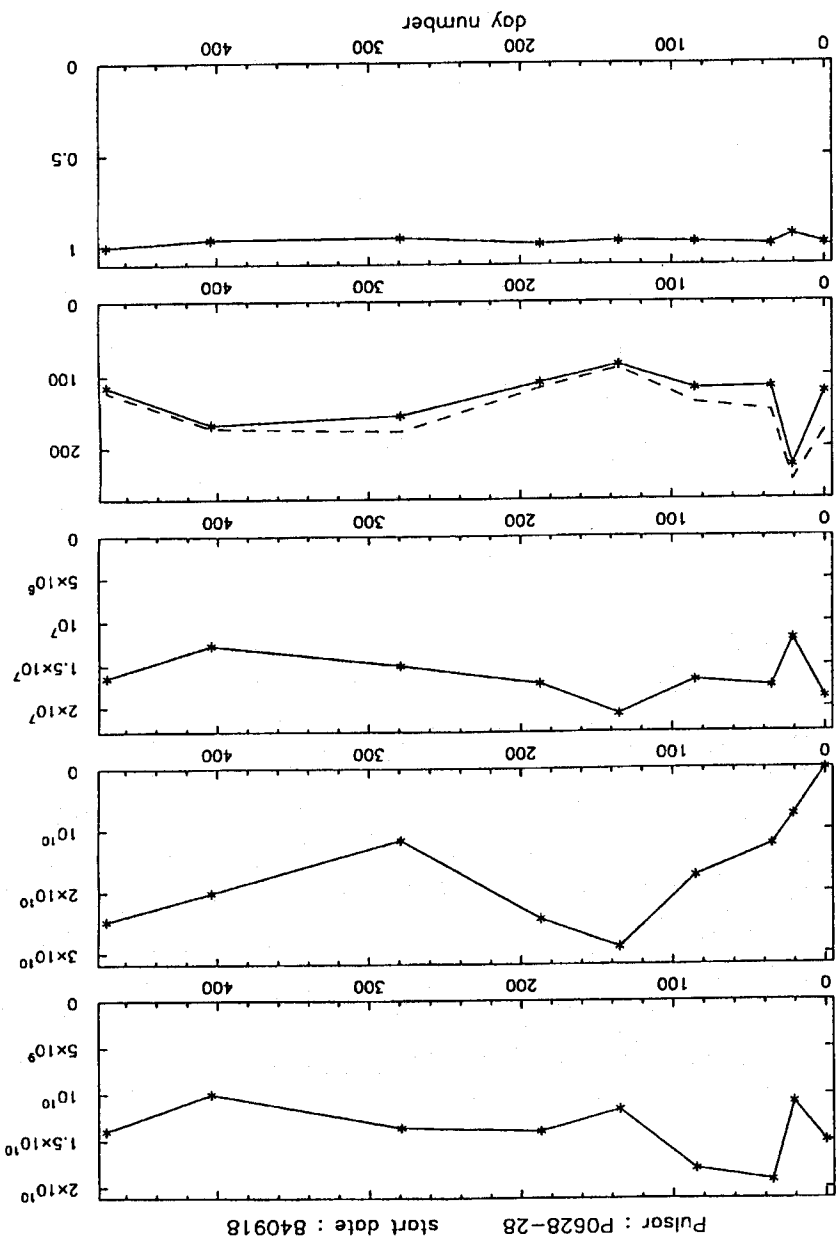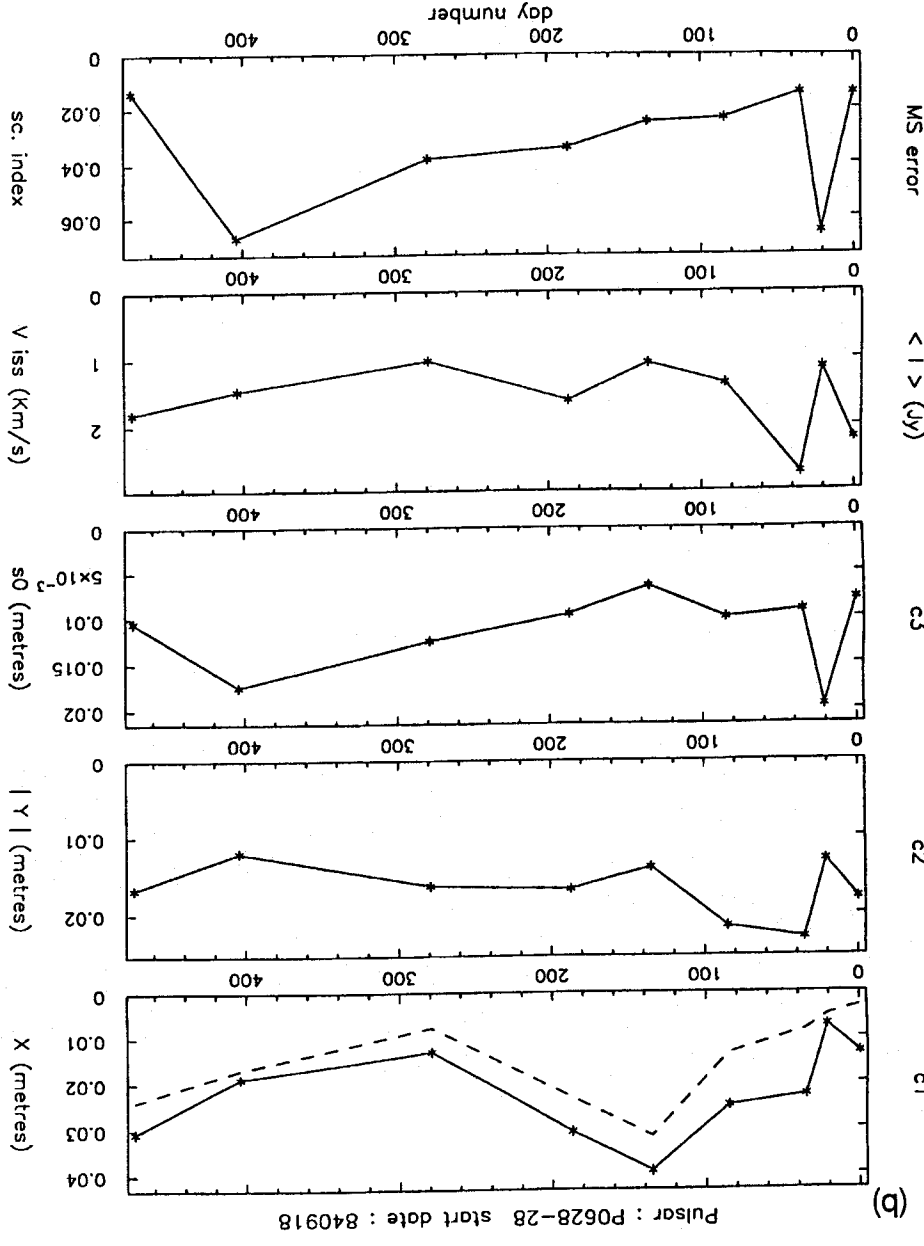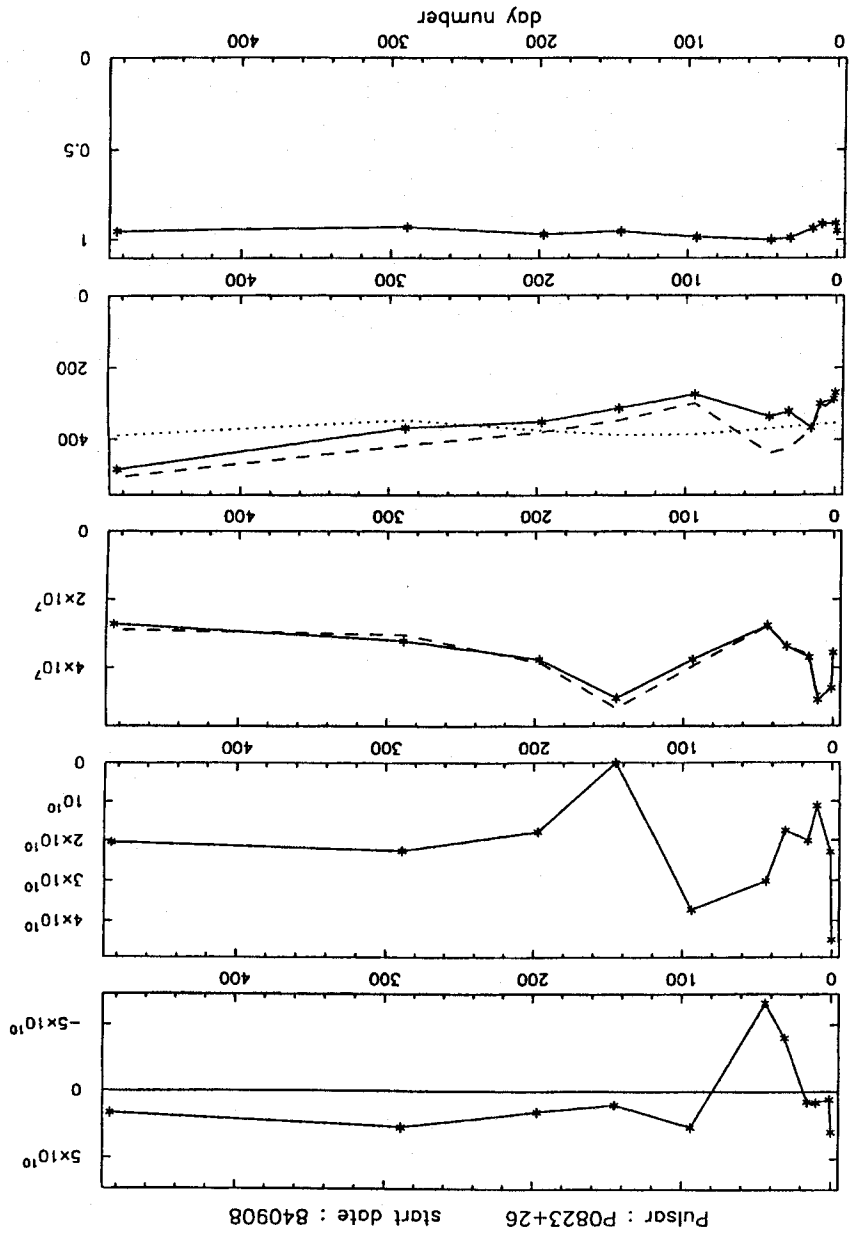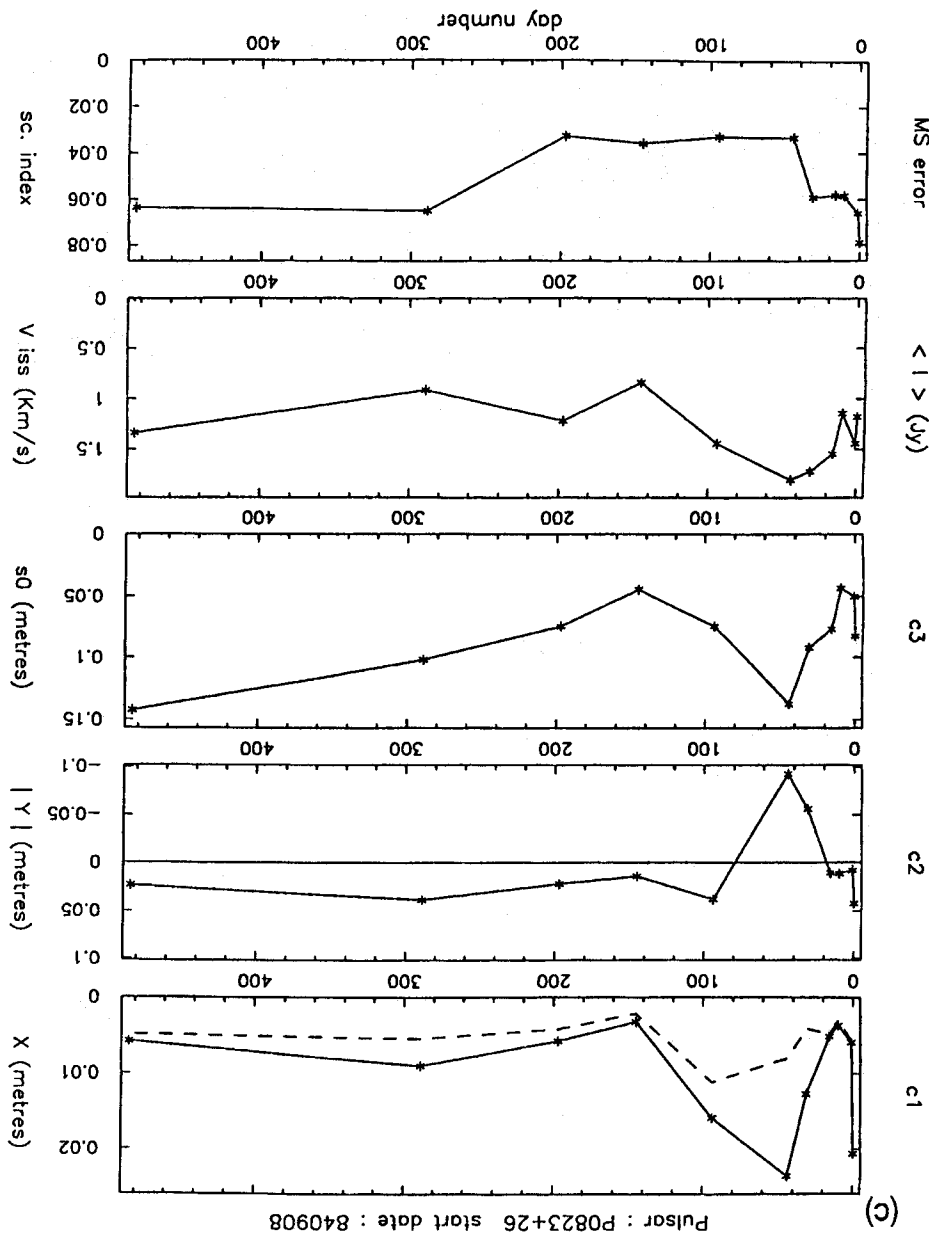
Pulsar : P0329+54   start date : 840909

Figure 3 – continued

Pulsar : P0628-28   start date : 840918

Figure 3 – continued

1050   *Y. Gupta, B. J. Rickett and A. G. Lyne*

Figure 3 – continued

Pulsar : P2016+28   start date : 840908

Pulsar : P2016+28   start date : 840908
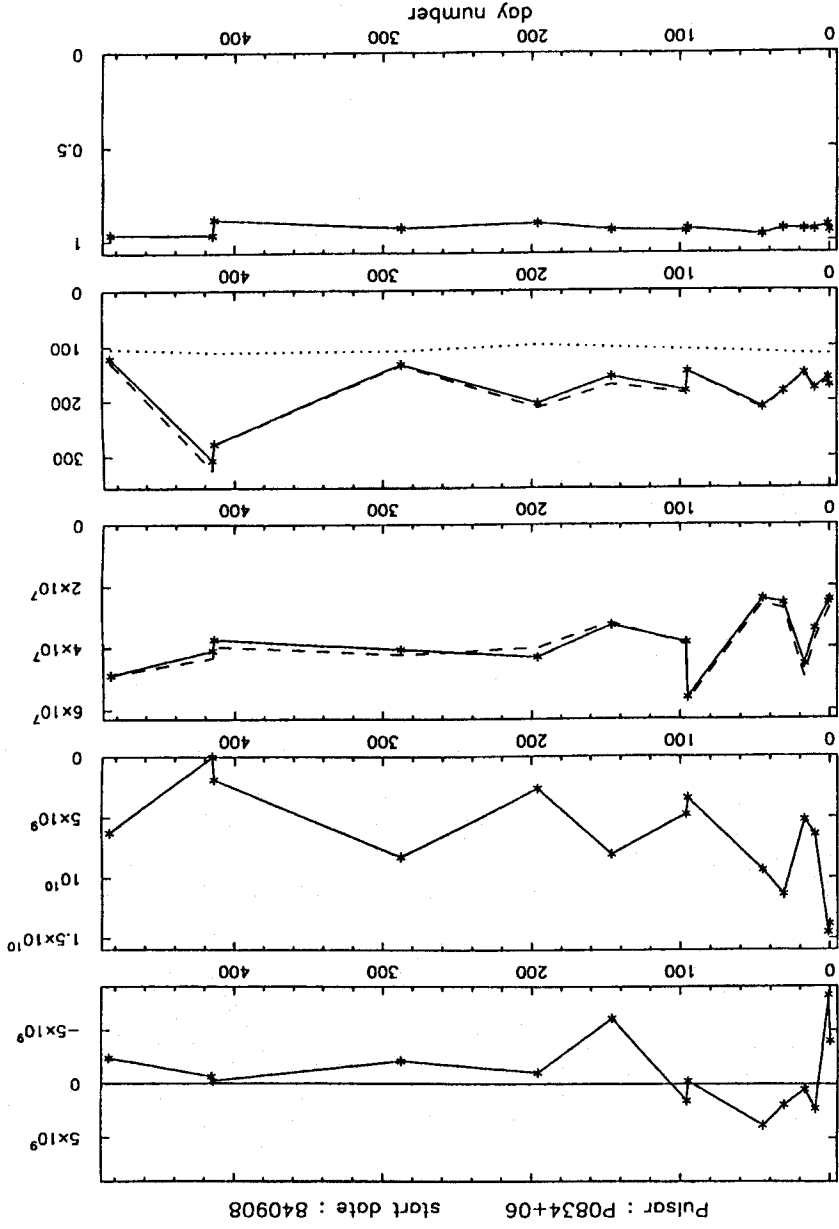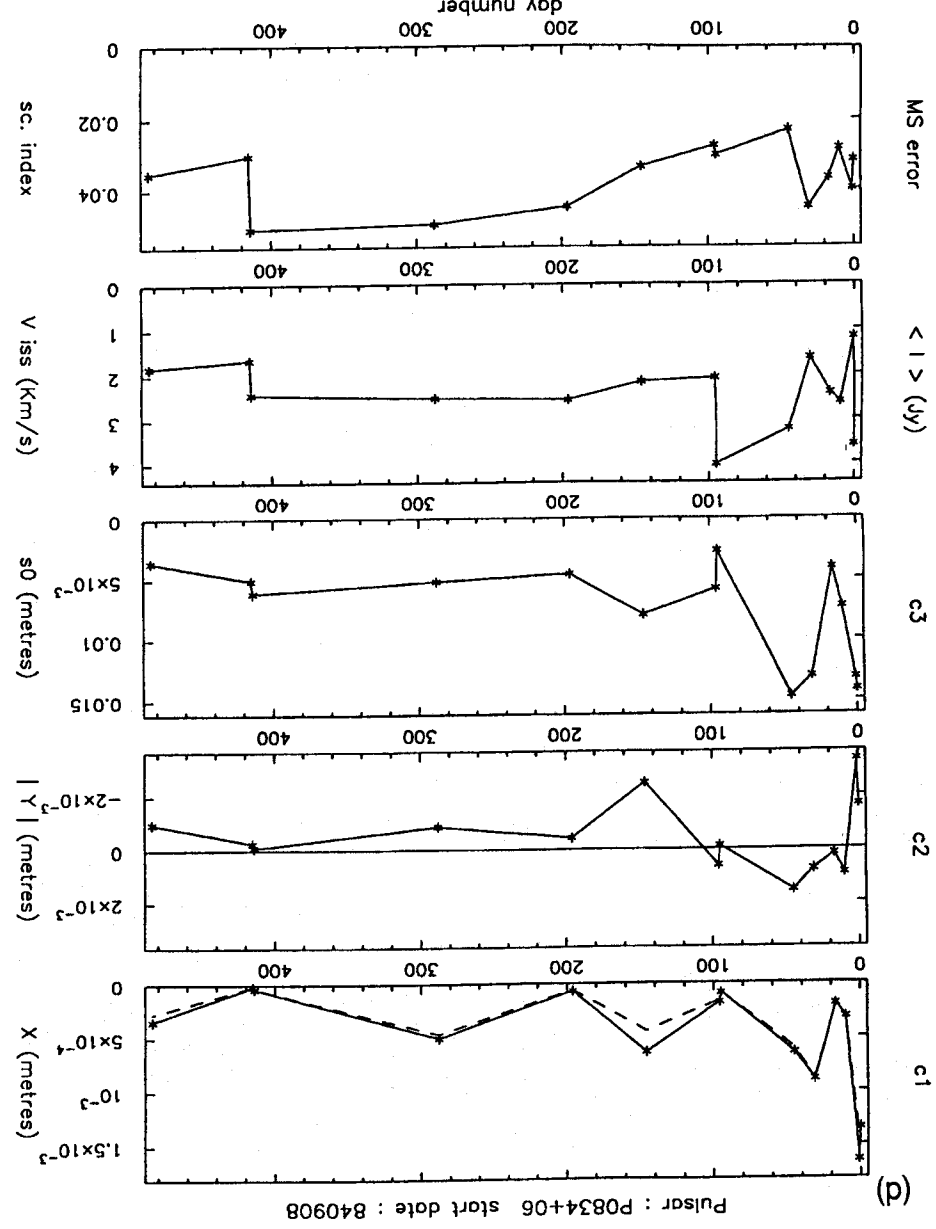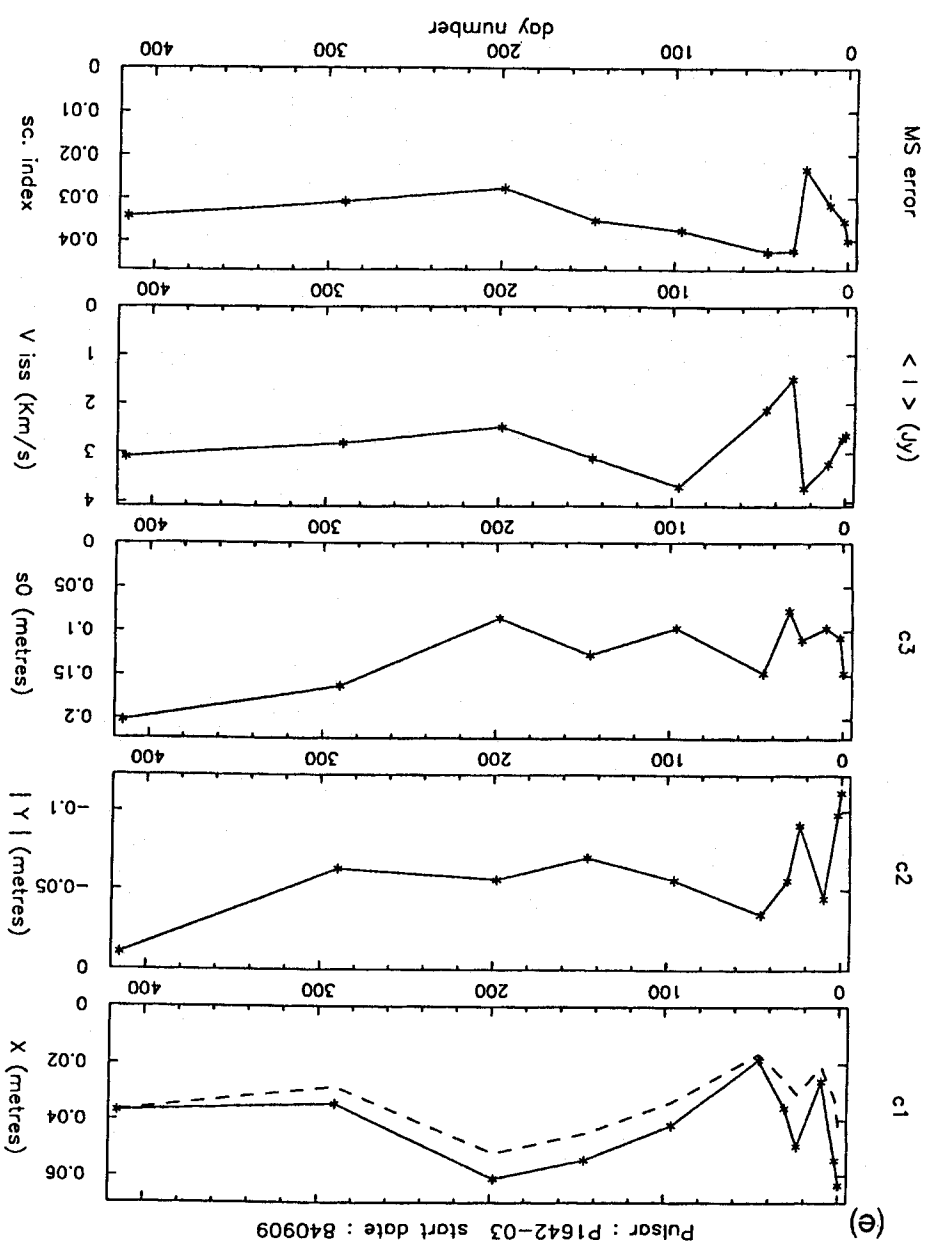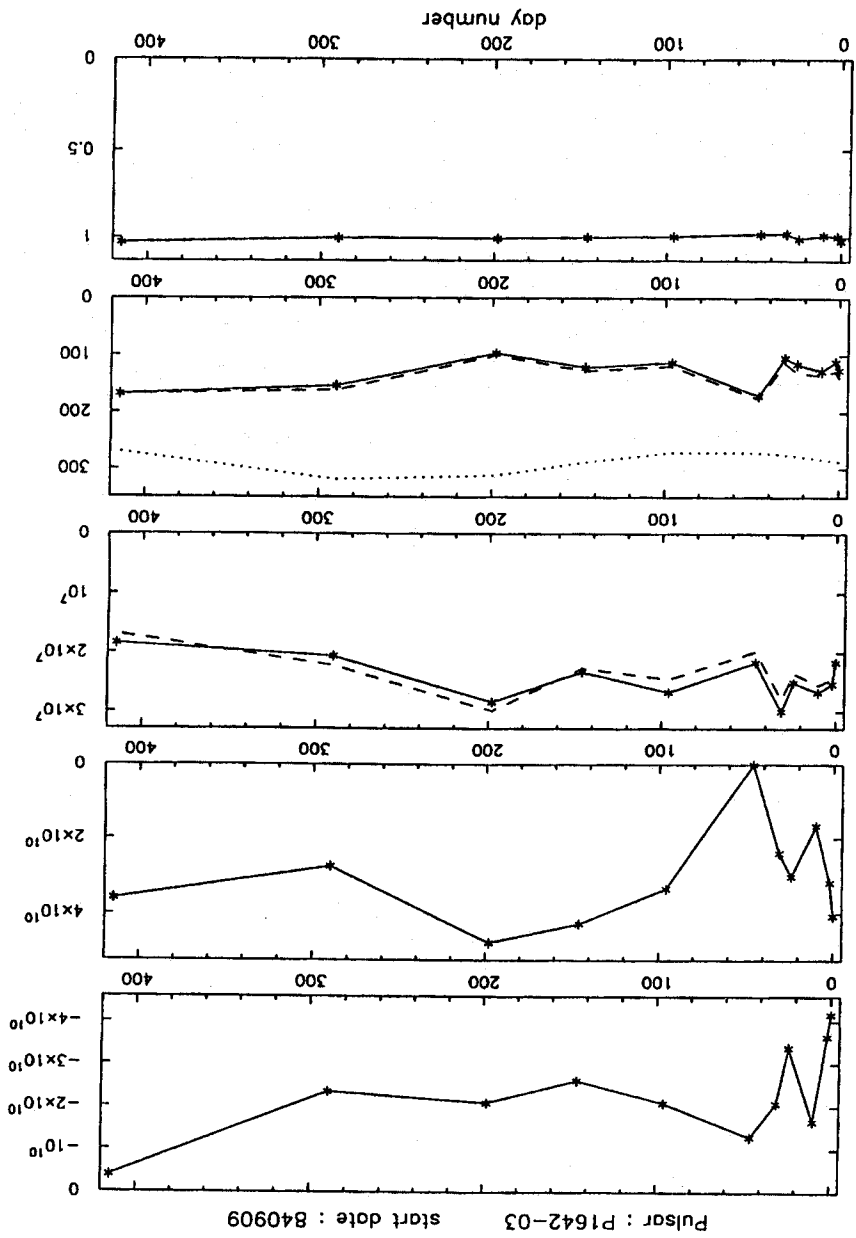
$$D_\phi(s_0) = 1 \; ; \quad \theta_d = 1/(k s_0) . \tag{3}$$

Note that this definition is not adequate for all forms of the wavenumber spectrum for the electron density. When the spectrum has a wavenumber exponent steeper than -4, a modified definition is required, since the phase gradient over s_0 is then likely to persist over a very large region (the 'outer scale'). Then the conditions for interference, which depend on the curvature of the phase, lead to an effective diffractive scale s_d, larger than s_0, and an instantaneous angular spectrum of width $\theta_d = 1/(k s_d)$. See Goodman & Narayan (1985) for a detailed discussion of this case. Under strong scintillation conditions, the spatial scale s_0 can be approximately related to the frequency scale ν_d and the Fresnel scale R_F as

$$\frac{\nu_d}{f} \approx \left(\frac{s_0}{R_F}\right)^2 = \frac{1}{u^2} , \tag{4}$$

where $R_F = (Z/k)^{0.5}$, at centre radio frequency $f = kc/2\pi$ and typical distance Z to the scattering irregularities. We introduce a strength of scattering parameter $u = R_F/s_0$, such that $u > 1$ defines strong scattering.

A consideration of the propagation equations shows that the field at a given observing point is influenced most strongly by a region whose lateral extent is about $Z\theta_d$. We call this the scattering disc but note that in an extended scattering medium there is a cigar-shaped scattering volume, which has a maximum radius of about $Z\theta_d$, where Z is the distance to the (point) source. (Note that some authors refer to $Z\theta_d$ as the 'multipath scale'.) The instantaneous angular spectrum of typical widt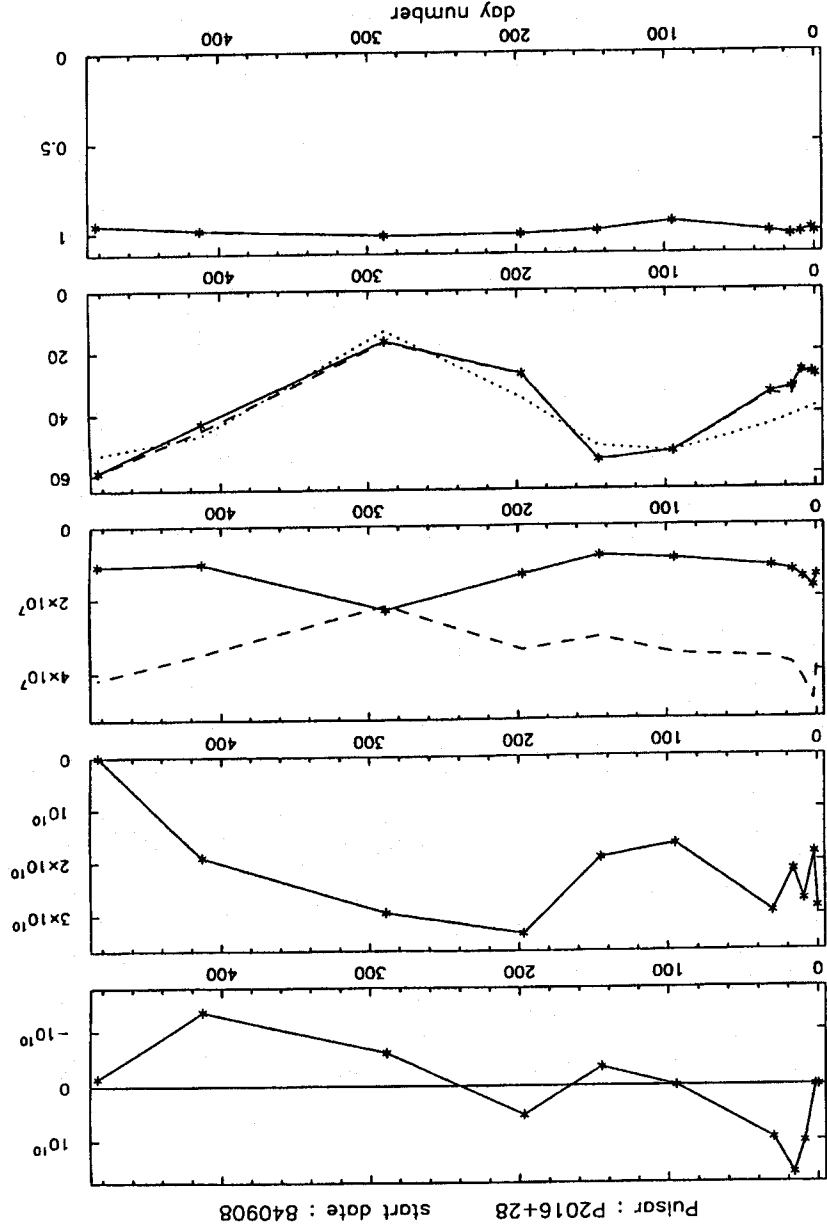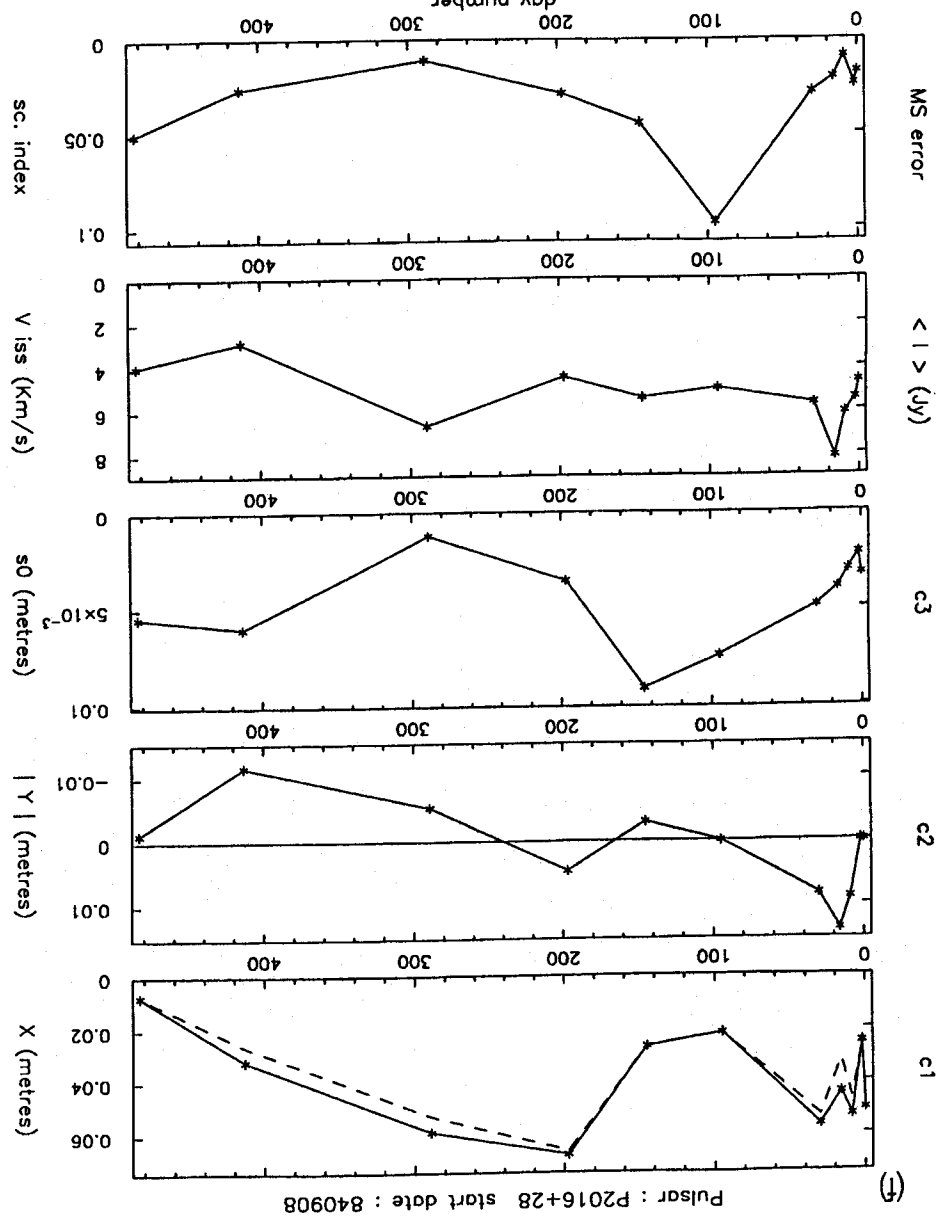h θ_d has a mean direction of arrival modified by the gradient of the phase ϕ averaged over the scattering disc. This gives a two-dimensional angle of refraction given by

$$\theta_r = (\theta_{rx}, \theta_{ry}) \approx \nabla\{\phi_r(s)\}/k . \tag{5}$$

Here $\phi_r(s)$ is the screen phase ϕ, smoothed over a scale of $Z\theta_d$, evaluated at $s = (x, y)$; alternatively, one can view $\phi_r(s)$ as derived from the same spectrum of irregularities as ϕ, but with an upper wavenumber cut off at about $(Z\theta_d)^{-1}$. Note that Cordes et al. (1986) represented this situation by scattering from a phase screen with components $\phi(s) = \phi_d(s) + \phi_r(s)$, where the 'diffractive phase' ϕ_d contains contributions from only those wavenumbers above $(Z\theta_d)^{-1}$.

The components of the angular spectrum interfere with each other and create a diffraction pattern with an approximately Gaussian probability distribution for the electric field at the observer's plane. This corresponds to an exponential probability distribution for intensity with rms variations equal to the (local) mean, and so unit scintillation index. These diffractive variations (scintles) have a characteristic spatial scale of approximately s_0, and a characteristic frequency scale ν_d, related as in equation (4). The local mean amplitude is controlled by the random refraction phase, ϕ_r. The first-order effect of ϕ_r is a lateral shift of the diffractive pattern, by a displacement $X \approx Z\theta_{rx}$, $Y \approx Z\theta_{ry}$. In second order, the curvature of ϕ_r causes a crowding together or spreading apart of the diffractive scintles, seen as amplitude variations over a larger scale (RISS). The refractive amplitude modulations can be approximately analysed using ray theory, providing that the fractional amplitude change is not large (i.e. no ray crossings); see Appendix B and Cordes et al. (1986). The typical scale of the refractive variations is given by the size of the scattering disc $Z\theta_d$, unless the spectrum of the electron
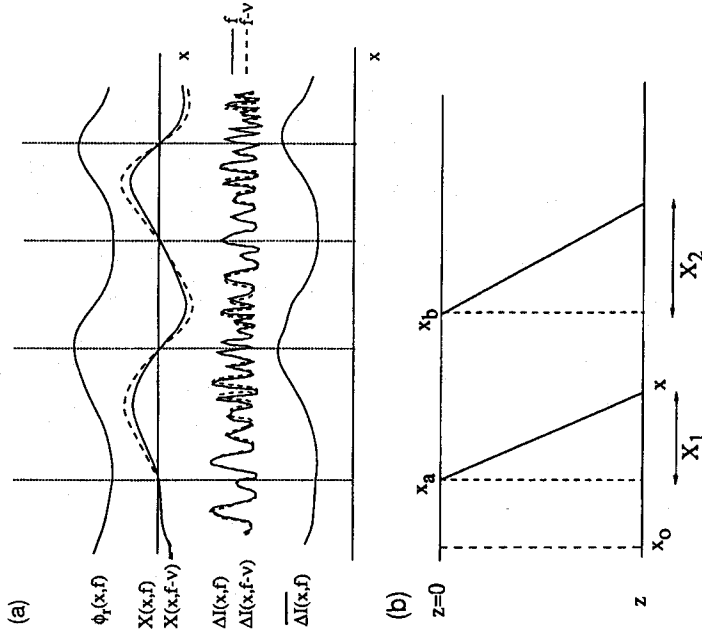
Figure 4. (a) Schematic representation (in one dimension) of the frequency-dependent refractive shifts of the diffractive scintillation pattern. ϕ_r is the refractive component of the phase due to a screen; X is given by equation (11) at two frequencies f and $f - v$ closer than the diffractive decorrelation bandwidth; ΔI is the diffractive intensity pattern at the two frequencies, displaced laterally by the appropriate shift X; $\overline{\Delta I}$ is the refractive intensity deviation averaged over many diffractive scintles. Note that diffractive peaks are offset between the two frequencies, corresponding to sloping features in the dynamic spectrum, which reverse in sign with the sign of X. Note also that the smallest offsets correspond to maximum or minimum refractive intensities. (b) One-dimensional version for the refracted 'ray paths' which pass through the screen at x_a and x_b, as used in Section 4.1.

density is a power-law function of wavenumber with an exponent steeper than -4. Thus $Z\theta_d$ determines the transverse scale over which X (and the refractive amplitude) will vary for the Kolmogorov spectrum, in particular. The presence of extra power at wavenumbers below $1/Z\theta_d$ would cause slower changes in the refractive displacements.

Since the refraction angle depends on frequency as f^{-2}, the refractive shift X also varies as f^{-2}. This is the basic cause of the drifting of the features in dynamic spectra (see Fig. 4a). If we consider observation of the dynamic spectrum at any epoch over a time long enough for a large number of diffractive scintles to have been sampled (or a wide enough bandwidth to include many scintles), the derived auto-correlation function (acf) of the intensity can be described as an average over the diffractive variations. For no refractive shift and no curvature, this normalized acf of diffractive intensity, as a function of spatial offsets ξ, η and frequency offset v, is defined as

$$C_d(\xi, \eta, v) = \frac{<\Delta I(x, y, f)\Delta I(x + \xi, y + \eta, f + v)>}{<\Delta I(x, y, f)^2>} , \tag{6}$$

where $<>$ denotes an average over very many diffractive scales and $\Delta I = I - <I>$ is the deviation of intensity from the local mean. Assuming a relative velocity between the pattern and

the observer of $V = \hat{x}V_x + \hat{y}V_y$, the spatial lags are mapped into temporal lags. Here the pattern is assumed 'frozen', so that the intrinsic temporal decorrelation of the intensity pattern is much slower than that caused by the convection of the pattern with relative velocity V. Under conditions of a refractive shift and motion of a frozen pattern, the intensity correlation at a single antenna at (x,y) versus offsets ν in frequency and τ in time becomes

$$C_r(\nu,\tau) = \langle \Delta I(x - X_1, y - Y_1, f)$$
$$\times \Delta I(x + V_x\tau - X_2, y + V_y\tau - Y_2, f + \nu)\rangle, \qquad (7)$$

where the refractive shifts are $X_1 = X(x_a, y_a, f)$ and $X_2 = X(x_b, y_b, f+\nu)$ and similarly for Y_1 and Y_2. This is illustrated for the one-dimensional case in Fig. 4(b). x_a, y_a are the coordinates of the point on the screen through which the 'ray' reaching location (x,y) at frequency f passes. x_b, y_b are the corresponding coordinates for the offset path. C_r can be expressed in terms of C_d, using equation (6), as

$$C_r(\nu,\tau) = C_d(V_x\tau + X_1 - X_2, V_y\tau + Y_1 - Y_2, \nu). \qquad (8)$$

This gives an approximate expression linking the intensity correlation function, including refractive shifts, to the purely diffractive correlation function. The shape of the intensity correlation function now depends on the refractive shift specific to the epoch under consideration.

4.2 RISS effects with linear refractive phase front

Since the refractive phase is taken to be varying slowly over the scale of the scattering disc size, it can be expanded as a Taylor series around a reference point for each epoch (Cordes et al. 1986). Taking $r_0 = (x_0, y_0)$ as the reference point, the refractive phase can be written as

$$\phi_r(x,y) = \phi_0 + \phi_x(x-x_0) + \phi_y(y-y_0) +$$
$$\frac{1}{2}\phi_{xx}(x-x_0)^2 + \frac{1}{2}\phi_{yy}(y-y_0)^2$$
$$+ \phi_{xy}(x-x_0)(y-y_0) + \cdots, \qquad (9)$$

where the various derivatives of ϕ_r are defined as

$$\phi_0 = \phi_r(x_0,y_0), \quad \phi_x = \frac{\partial\phi}{\partial x}\bigg|_{(x_0,y_0)}, \quad \phi_y = \frac{\partial\phi}{\partial y}\bigg|_{(x_0,y_0)},$$
$$\phi_{xx} = \frac{\partial^2\phi}{\partial x^2}\bigg|_{(x_0,y_0)}, \quad \phi_{yy} = \frac{\partial^2\phi}{\partial y^2}\bigg|_{(x_0,y_0)},$$
$$\phi_{xy} = \phi_{yx} = \frac{\partial^2\phi}{\partial x\partial y}\bigg|_{(x_0,y_0)}. \qquad (10)$$

A useful first approximation is to linearize the slowly varying refractive phase front by neglecting the second and higher order derivatives in equation (9) and consider the effect on the diffractive scintillation pattern. The refractive shift is given by

$$X = \frac{Z}{k}\frac{\partial\phi_r(x,y)}{\partial x} = R_F^2\phi_x ;$$
$$Y = \frac{Z}{k}\frac{\partial\phi_r(x,y)}{\partial y} = R_F^2\phi_y . \qquad (11)$$

Evidently, under the linear phase front assumption, the refractive shift is not a function of the position on the screen. However, since $\phi_r(x,y)$ itself varies directly with wavelength,

the refractive shift is inversely proportional to the square of the frequency and

$$\frac{\partial X}{\partial f} = -\frac{2X}{f}. \qquad (12)$$

Under these conditions, a diffractive intensity maximum is shifted to different locations in the observing plane at different frequencies. Relative motion of an observer with a velocity V through such a scintillation pattern maps the spatial separation between intensity features at different frequencies to a temporal delay. This gives rise to the characteristic drift of the features in the dynamic spectra. Furthermore, the refractive shift will also reduce the correlation of the intensity at frequency offset ν and zero time offset. Thus the effective correlation bandwidth of the scintillation features is reduced. With slow and random variations of the gradient of the refractive phase fluctuations at the screen, the refractive shift should fluctuate in magnitude and direction, leading to random variations, with epoch, of the slope of the features and the frequency decorrelation width.

Using equation (12), $X_1 - X_2$ can be expressed as

$$X_1 - X_2 = \frac{2X\nu}{f}, \qquad (13)$$

where X is evaluated at the frequency f ($\nu = 0$). Using a similar expression for $Y_1 - Y_2$, the final expression relating the acf under conditions of linear refractive phase with that under purely diffractive conditions becomes

$$C_r(\nu,\tau) = C_d\left(V_x\tau + \frac{2X\nu}{f}, V_y\tau + \frac{2Y\nu}{f}, \nu\right). \qquad (14)$$

The problem now reduces to finding an expression for C_d. This involves computation of the generalized fourth moment of the electric field at the observing plane. The problem has been attacked by several authors (Codona et al. 1986c; Lee & Jokipii 1975), and solutions have been found for special conditions; but no complete, generalized expression is available. Two different models are investigated here – the Gaussian-elliptical model and the square-law (Shishov) model.

A simple and useful model for C_d is provided by a Gaussian-elliptical model, specified as

$$C_d(\xi,\eta,\nu) = \exp\left(-\frac{\xi^2+\eta^2}{s_0^2} - \frac{\nu^2}{\nu_d^2}\right); \qquad (15)$$

where s_0 is the spatial decorrelation width (coherence scale) and ν_d is the decorrelation bandwidth. Using equation (14), this yields the two-dimensional Gaussian in equation (2), where the parameters c_1, c_2 and c_3 are given by

$$c_1 = \frac{4(X^2+Y^2)}{f^2 s_0^2} + \frac{1}{\nu_d^2};$$
$$c_2 = \frac{4(XV_x + YV_y)}{f s_0^2};$$
$$c_3 = \frac{V_x^2 + V_y^2}{s_0^2}. \qquad (16)$$

In the simple Gaussian-elliptical model, contours of constant correlation are ellipses in the (τ,ν) plane. The correlation function along either the τ or ν axis is a Gaussian. $1/\sqrt{c_1}$ and $1/\sqrt{c_3}$ estimate the $1/e$ decorrelation widths in frequency and time, respectively. In the absence of any refractive effects ($X = Y = 0$), $c_2 = 0$ and the major axis of the ellipse is aligned along the τ and ν axes. With non-zero values for X or

Y, the cross-term c_2 becomes positive or negative, according to equation (16), and this is seen as a tilt of the ellipse with respect to the τ, ν axes. Also, the value of c_1 increases, leading to a decrease in the observed decorrelation bandwidth. Due to their dependence on the refractive shift components X and Y, c_1 and c_2 are expected to vary slowly and randomly as the pulsar relative velocity is dominated by the proper motion velocity of the pulsar itself and can be assumed constant, and thus c_3 should remain relatively constant. Although the Gaussian model of equation (15) is not well justified theoretically, we use it because the resulting correlation in frequency and time, equation (2), is well suited for fitting since it has only three parameters. Of the models derived from wave propagation theory, the simplest one for C_d corresponds to a square-law structure function (Chashei & Shishov 1976). This is discussed in Appendix A, where expressions for its four parameters are given in the presence of the refractive shifts X,Y. We found no worthwhile improvements in the fit to the correlations in using this model. In Appendix B we also give an elaboration of the Gaussian model, in which the refractive perturbation is modelled by a curved wavefront. We now apply the theoretical ideas developed above to the interpretation of the results displayed in Fig. 3.

5 INTERPRETATION OF RESULTS

5.1 Estimation of the scattering parameters

Without any loss of generality, the x and y axes in equations (9) to (16) can be oriented such that the x axis is parallel to V, making $V_y = 0$. This simplifies the expressions in equation (16) and allows us to invert them and obtain estimates of s_0, v_d, X and Y, provided that the velocity is known. X, $| Y |$ and s_0 estimated in this fashion are displayed as time series for each pulsar in the right hand panels of Figs 3(a)-(f). The value of s_0 is estimated from each value of c_3 and the velocity, which is taken as the proper motion velocity, where available, and as the scintillation velocity from Cordes (1986) otherwise. The dashed line plot of s_0 comes from adding the effect of the changing Earth velocity to the proper motion velocity. Only for PSRB2016+28 does it make a difference, as discussed below. X is obtained from the expression for c_2 and the mean s_0. We also define c_{1Y} as

$$c_{1Y} = c_1 - \frac{c_2^2}{4c_3} = \frac{1}{v_d^2} + \frac{4Y^2}{f^2 s_0^2}. \qquad (17)$$

c_{1Y} is plotted, as a dashed line, together with c_1 in the top left panels of Fig. 3. This correction is only substantial for PSRB0823+26. It is interesting that the associated decorrelation bandwidth, $1/\sqrt{c_{1Y}}$, corresponds mathematically to the characteristic bandwidth measured along the drift line, as used by Lyne & Smith (1982). Here we use the minimum value of c_{1Y} to estimate $v_d = 1/\sqrt{c_{1Y min}}$, assuming that the minimum occurs where Y approaches zero. Finally Y^2 is estimated from

$$Y^2 = 0.25 f^2 s_0^2 (c_{1Y} - c_{1Y min}). \qquad (18)$$

Thus $|Y|$ is plotted with, by definition, a minimum value of zero.

In the bottom right panels of Fig. 3 we plot the measured scintillation index $\delta I_{rms}/ < I >$. It is not significantly different from unity, in agreement with expectations for diffractive scintillations normalized by the 'local' mean intensity. Note that it does not include the extra variance due to the slower refractive variations.

In the fourth right hand panels of Fig. 3 we also plot the scintillation velocity for each observation. The scintillation velocity is usually calculated using the definition of Cordes (1986) equation (6). As discussed in Appendix C, we have used a formula that gives a value larger than his by a factor of 3:

$$V_{ISS} = 3.8 \times 10^4 \times \frac{[(v_{d,MHz})(D_{kpc})]^{0.5}}{[(f_{GHz})(\tau_{d,s})]} \text{ km s}^{-1}. \qquad (19)$$

D_{kpc} was taken from Cordes (1986); estimates of $v_{d,MHz}$ and $\tau_{d,s}$ were made from the individual values of c_1 and c_3. Note that v_d was estimated at a correlation of 0.5, while τ_d was estimated at $1/e$, in accordance with the convention used by Cordes (1986). An additional estimate of V_{ISS} was made using c_{1Y} in place of c_1. This is plotted as a dashed line in the fourth right hand panel, but in no case does it make a substantial difference. Also shown by a dotted line is the expected speed based on the measured proper motion velocity (Lyne et al. 1982) added vectorially to the Earth's velocity with respect to the Sun. There is reasonable agreement for most of the pulsars except PSRB0329+54 and PSRB1642-03, for which the scintillation velocity is substantially below the proper motion velocity. Here a possible explanation is that the scattering is concentrated in a layer which is asymmetrically placed, so that $x \neq 1$ in equations (C12) to (C16). For a layer near the pulsar ($x > 1$) equation (C15) gives an increase as x in the $\sqrt{x}$ in the observed value. Thus a layer closer to the Earth ($x < 1$) could resolve the discrepancy. Alternatively, equation (C15) shows that the predicted velocity can be reduced by an appropriate magnitude and direction for the screen velocity, which is assumed to be zero for the plots in Fig. 3. PSRB2016+28 presents a special case, in which the Earth's velocity is comparable to the proper motion velocity and substantially modulates the net pattern velocity. This case is discussed in more detail below.

5.2 Comparison of observed and predicted parameters

In the model of equation (16) the parameter c_3 (and the derived s_0 estimator) should be approximately constant. In contrast, variations are expected in c_1, which should be partially correlated with those of c_2. The values of X and Y should both be comparable to the rms value given by equation (5). The scintillation velocities should be close to the proper motion velocities. In considering how results for each pulsar compare with theory, we start by classifying the parameter variations for each object. In Table 2 we give the modulation index (= rms/mean) for each of the c-parameters. The approximate percentage error in a *single* observation, due to the finite duration of the data set, is given in column 7. The error is simply given by $100/\sqrt{N}$, where N is the number of scintles in a typical dynamic spectrum for each source. N is taken to be $BT/(4v_d\tau_d)$, where T is the observing time (60-300 min) and B is the bandwidth covered (5 MHz). The factor 4 gives an approximate estimate of the 'density' of the scintles; note that Cordes (1986) more conservatively uses a value 100 for this

Table 2. Variability of scintillation parameters.

Pulsar	c_1	Modulation index of:			Int	% err	Class	u
		c_{1Y}	c_2	c_3				
P0329+54	0.52	0.46	4.2	0.32	0.40	14	VS,VT	80
P0628-28	0.43	0.62	0.21	0.36	0.33	36	FS,-	37
P0823+26	0.67	0.59	7.6	0.38	0.22	24	VS,VT	34
P0834+06	1.0	0.99	2.9	0.53	0.53	100	-,-	10
P1642-03	0.32	0.30	0.44	0.29	0.22	12	FS,VT	57
P2016+28	0.45	0.45	5.2	0.49	0.25	38	VS,VT	46

factor. The data for PSRB0834+06 do not include enough scintles to be statistically useful and so are not considered in subsequent analysis, even though this pulsar exhibits intriguing structures in its dynamic spectra. The last column is our estimated scattering strength u, estimated as described below. The modulation index of c_1 is typically 30-60 per cent, with similar values for c_{1Y}; this corresponds to 15-30 per cent variation in apparent scintillation bandwidth. For PSRB0628-28 and PSRB1642-03 there are 21 and 44 per cent variations in c_2; in contrast PSRB0329+54, PSRB0823+26 and PSRB2016+28 have very large modulation indices for c_2, representing the fact that c_2 varies in sign, making the estimated mean small. These three pulsars thus conform to our expectation that c_2 should vary in amplitude with a zero mean, whereas the other two do not. The time-scale for variations of c_2 should be equal to the time-scale for RISS. For PSRB2016+28 this is 68 d, compatible with the apparent time between sign reversals in c_2. However, for PSRB0329+54 and PSRB0823+26 the RISS times are 7 and 2 d, respectively, which are very much shorter than the apparent time between sign reversals in c_2. The sparse sampling prohibits further exploration of this possibility. If confirmed it would suggest that the refraction angle changes more slowly than expected, raising interesting possibilities that there are large refracting structures in the line of sight which do not have enough phase curvature to cause intensity modulation. This appears to be the explanation for PSRB0628-28 and PSRB1642-03. The variations in c_3 are 29-38 per cent, when PSRB0834+06 is ignored and PSRB2016+28 is treated separately. It is clear that c_1 is significantly more variable than c_3, but that there are c_3 variations in excess of statistical uncertainty for PSRB0329+54, PSRB0823+26, PSRB1642-03 and PSRB2016+28. Thus we classify the objects with variable sign of slope as class VS and a fixed sign of slope as class FS; those with significant variations in time-scale we call class VT. The classifications are also indicated in Table 2, where they are thought to be significant. The intensity variations are 10-50 per cent, but are not of immediate interest.

We now compare the estimated magnitudes of X, Y and s_0 with values expected for a simple Kolmogorov model of the density spectrum. The results are presented in Table 3. Assumed parameters are pulsar distance from Cordes (1986), proper motion speed (V_{pm}) from Lyne et al. (1982) and R_F at 408 MHz. The predicted parameters can be expressed in terms of the scale R_F and the strength of scattering parameter u. We use our v_d, estimated as decribed above, with equation (4) to determine u, the strength of scattering parameter, which is listed here as a predicted parameter. The predicted s_0 is then R_F/u. The average measured values of the parameter s_0 are within a factor 0.31 to 1.2 of the predicted values. This

comparison is closely related to a comparison of V_{ISS} and the proper motion velocity. The scintillation velocity is given in the last column as the average of the values plotted in Fig. 3, with the standard deviation expected for a single observation. The predicted rms values of X and Y can be estimated from equation (5) and the distance, Z. The rms refractive phase gradients, averaged over the scattering disc, can be found from the structure function, giving the following expression for the rms value of X:

$$X_{rms} = R_F^2 \frac{[D_\phi(s_r)]^{1/2}}{s_r} \approx u^{2/3} R_F = u^{-1/3} s_r, \qquad (20)$$

where $s_r = u^2 s_0$ is the refractive scale. The measured X and Y values are given as the root of the mean square, without correction for the mean. The agreement with the predictions is within a factor 2 or better, which constitutes a definite success for the model. The last column of Table 3 is the average of the scintillation velocity from the different epochs as plotted in Fig. 3. The two entries in Table 3 for PSRB1642-03 correspond to different assumed distances, and are discussed below.

The most notable failure is the variability of c_3 and the associated scale s_0. The obvious example is PSRB2016+28, for which the changing Earth velocity is an important factor, as discussed below. However, for most of the other pulsars the contribution of the Earth's velocity to the total relative velocity is negligible and other explanations are called for. In some cases the model is unable to fit the correlation function very well as the contours of constant correlation are not exactly elliptical in shape. These fits are characterized by larger than usual mean square errors. In this data set, it happens primarily for PSRB2016+28 during epochs where periodic patterns dominate the dynamic spectra. As discussed below, more detailed models of the refractive phase fluctuations including local curvature can provide an explanation for some of the variations of the temporal correlation width and also of the intensity.

5.3 The visibility of the slopes and variations of the scintillation bandwidth

One of the motivations of our observations was to characterize and monitor the sloping features in the dynamic spectra. We define here a visibility index for the sloping features. The angle of slope of the fitted ellipse is clearly not useful since it depends on the plotted scales. Other choices are slopes dT/dv or dv/dT. Consider the estimation of dT/dv for the fitted ellipse. The first thought is to find the slope of the the major axis of the ellipse in a (v, τ) plot and scale it by the time and frequency scales. However, this method is not satisfactory since its value depends on the plotting scales. Another method is to find the dT/dv slope of the line through the point on the ellipse furthest from the time axis; this is given by $-c_2/2c_3$. From equation (16), we note that c_2 should fluctuate about zero. Thus dT/dv by the second method is to be preferred over its reciprocal, which has often been used to characterize such observations. However, dT/dv does not give an indication of the visibility of the slopes, until it is normalized to the characteristic time and frequency scales.

Consider the ellipse $(c_1 v^2 + c_2 v\tau + c_3 \tau^2) = 1.0$ expressed in terms of normalized coordinates $y = v\sqrt{c_1}$ and $x = \tau\sqrt{c_3}$ as

$$x^2 + 2rxy + y^2 = 1, \quad \text{where } r = \frac{c_2}{\sqrt{4c_1 c_3}}. \qquad (21)$$

Table 3. Predicted and measured scintillation parameters.

	Assumed Parameters			Predicted Parameters			Measured Parameters			
Pulsar	Z (kpc)	V_{pm} (km s^{-1})	R_f (10^9 m)	u	S_0 (10^7 m)	X_{rms} or Y_{rms} (10^{10} m)	S_0 (10^7 m)	X_{rms} (10^{10} m)	Y_{rms} (10^{10} m)	$\overline{V}_{iss}$ (km s^{-1})
P0329+54	2.30	229	2.88	80	3.6	5.3	4.4	5.7	11.	160±26
P0628-28	1.30	111	2.17	37	5.8	2.4	3.2	1.4	1.9[1]	106±10
P0823+26	0.71	365	1.60	34	4.7	1.7	3.7	2.9	2.5	330±58
P0834+06	0.43	104	1.25	10	12	0.58	3.7	0.34	0.80	180±50
P1642-03a	1.3	293	2.17	57	3.8	3.3	2.4	2.6	3.3[1]	376±70
P1642-03b	0.16	36	0.74	57	1.3	1.1	0.27	0.3	0.38	130±24
P2016+28	1.3	15	2.17	46	4.7	2.8	1.3	0.8	2.4	36±13

[1] These values will be underestimated, since no sign reversals of slopes were seen.

In the x,y plane this is an ellipse tilted at 45°. Expressed as a $dT/d\nu$ slope in s Hz^{-1}, we obtain $-r\sqrt{c_3}/\sqrt{c_1} = -c_2/2c_3$, as above. The ellipse has an axial ratio $\sqrt{1+|r|}/\sqrt{1-|r|}$, which determines the visibilty of the sloping features. A large axial ratio corresponds to prominent slopes and unity axial ratio corresponds to symmetrical features. We use $p = r^2$ as a visibility index for the slopes:

$$p = r^2 = \frac{c_2^2}{4c_1c_3}.$$ (22)

The value of p is readily found for each data set and the mean values are listed in Table 4. Using the model of equation (16), we can also estimate the expected value of p. An approximate result (derived in Appendix D) is

$$<p> \approx \frac{0.5}{1+0.125\,u^{2/3}}.$$ (23)

The conclusion is that $<p>$ will be about 0.5 for u near 1, which corresponds to highly visible sloping features. Examples are given for interplanetary scintillation in the data of Cole & Slee (1980). As u increases, p decreases but p does not drop below 0.25, until u is greater than about 25. Table 4 lists both the mean measured value and the prediction from equation (23). The predicted values are in the range 0.15-0.32, whereas the observed values cover 0.07-0.4, with estimated errors of about 30 per cent. The expected decrease of p with increasing u is not seen in our observations. For PSRB1642-03 and PSRB0628-28, c_2 does not change sign and this already shows that they are not consistent with the model. For PSRB0834+06 the estimation errors are very high, making p very uncertain. But even the remaining three pulsars do not show a strong trend versus u. PSRB0329+54 shows the smallest measured value u (0.07) and it has the largest u, but it is well below the predicted value (0.15). In summary, the model is only partially successful in predicting the visibility of drifting bands and how it varies with strength of scattering.

Turning now to variations in the apparent scintillation bandwidth, we can again make use of the varying refraction model. Consider simultaneous observations at two frequencies, for which the diffractive scintillations should be highly correlated. The effect of a refractive shift is to displace the diffraction patterns at the two frequencies by different amounts; this will decorrelate the variations, and so reduce the apparent decorrelation bandwidth. Referring to equation (16), we define the apparent scintillation bandwidth as $\nu_{d,app} = 1/\sqrt{c_1}$. In Appendix D, we derive its mean and standard deviation, under the assumption that the shifts X and Y are independent Gaussian zero mean random variables, with variance given by the square of equation (20). Fig. 5 shows how $<\nu_{d,app}>/\nu_d$ is biased below unity as a function of the strength of scattering u. The dotted lines are the mean ± one standard deviation and so show a typical range of bias for an isolated observation. The dashed line gives the modulation index for $<\nu_{d,app}>$. These plots should be of use to other investigators concerned with the bias and stability of measured decorrelation bandwidths and so of scintillation velocity, for which the modulation index would be half of that shown.

There is an associated conclusion about the theoretical form for the correlation function of intensity versus frequency. It is conventionally approximated by the square of the second moment after the delay term is removed (Lee & Jokipii 1975). The refractive shifts become unimportant if p in equation (22) is small, i.e. when $u \gg 20$. If this condition is not met, the more precise form calculated (for a screen geometry) by Codona et al. (1986c) should be used. Consequently, estimates of the exponent α made from the shape of the correlation function (e.g. Armstrong & Rickett 1981) will only be valid for similarly large values of u.

Our results are summarized in Table 4. In column 2 is the decorrelation bandwidth reported by Cordes (1986), scaled to 408 MHz according to $\nu_d \propto f^{4.4}$. Columns 3 and 4 give the mean of the 'apparent' decorrelation bandwidth and the standard deviation of a single measurement; column 5 gives the maximum apparent bandwidth; column 6 gives the adopted value based on c_{1Ymin}, as described in Section 5.1; column 7 gives the mean diffractive decorrelation time. Column 8 gives u estimated from column 6 and equation (4); columns 9 and 10 give the predicted and measured modulation indices (rms/mean) in the apparent decorrelation bandwidth, as discussed below. The pulsars studied here have $10 < u < 100$, for which an isolated observation of $\nu_{d,app}$ interpreted as ν_d should give an underestimate by a factor of two or less, according to Fig. 5. In Table 4 this factor is estimated by the

Table 4. Estimates of diffractive scintillation parameters.

Pulsar	$\nu_{d,Cordes}$ kHz	$\bar{\nu}_{d,app}$ kHz	$\sigma_{d,app}$ kHz	$\nu_{d,app\ max}$ kHz	ν_d kHz	τ_{iss} sec	u	rms/mean $\nu_{d,app}$ pred.	rms/mean $\nu_{d,app}$ obs.	mean p pred.	mean p obs.
P0329+54	75	47	11	61	63	194	80	.12	.23	.15	.07
P0628-28	370	118	32	190	291	273	37	.17	.27	.21	.4
P0823+26	640	189	58	284	349	102	34	.18	.31	.22	.3
P0834+06	500	1260	960	3910	4390	355	10	.25	.76	.32	.1
P1642-03	74	82	16	119	126	82	57	.14	.20	.18	.2
P2016-28	122	92	34	189	190	462	46	.16	.38	.19	.07
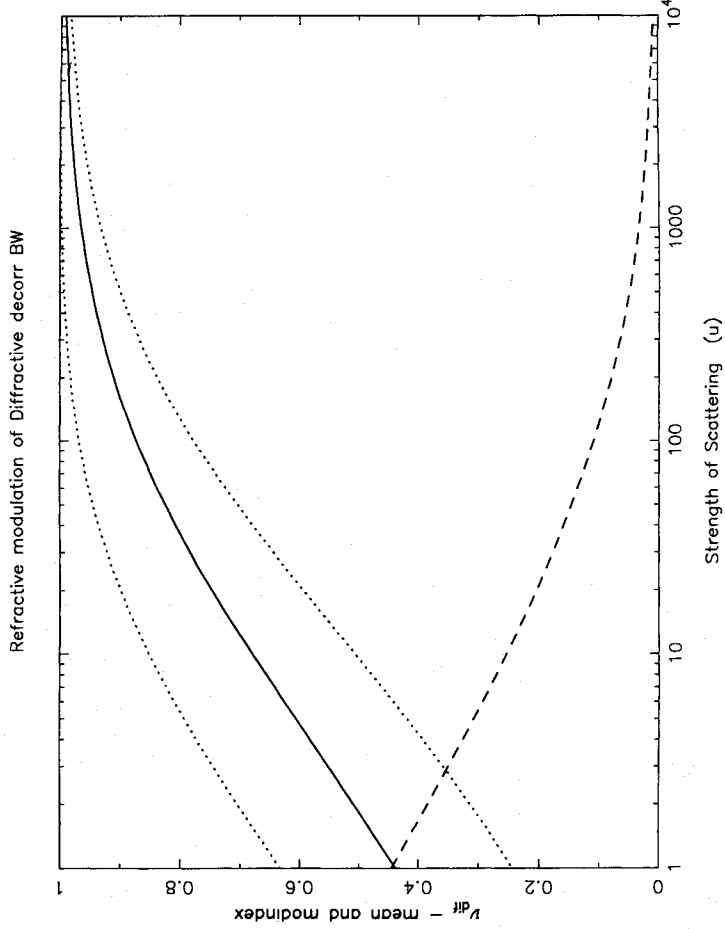
Figure 5. Theoretical bias and variability of the apparent diffractive decorrelation bandwidth versus strength of scattering u. The solid curve is the bias, expressed as the average apparent bandwidth over the 'true diffractive' bandwidth; the dotted lines are plus or minus one standard deviation and so give a typical range within which a single observation should lie. The dashed line gives the expected modulation index (rms/mean) for the apparent bandwidth.

ratio of ν_d to $\bar{\nu}_{d,app}$. The variability of the $\nu_{d,app}$ is indicated by its standard deviation in column 4; and in column 10 its modulation index is given and is to be compared to the theoretical value in column 9 from Fig. 5 at the given value of u. The observed values are greater than the expected values, but they confirm the prediction that the apparent decorrelation bandwidth becomes less variable as the strength of scattering increases. Our observations of PSRB0834+06 are particularly variable. Whereas it has the lowest value of u, we note that there was extra variability due to the fact that the observing bandwidth did not include many scintles, adding variability due to estimation error.

A comparison can also be made between our adopted decorrelation bandwidth and those published in the litera-

ture. ν_d (Table 4, column 6) should be compared with the value in column 2 from Cordes (1986). PSRB0329+54 and PSRB0628-28 give agreement; for PSRB0823+26 our value is substantially below Cordes' value; for PSRB1642-03 and PSRB2016+28 our values are about twice Cordes'; for PSRB0834+06 our value is 10 times Cordes'. Measurements by Roberts & Ables (1982) found its bandwidth to be highly variable, in agreement with our results. Important conclusions of our work are the variability of the apparent decorrelation bandwidth and the increase of variability as the strength of scattering decreases. A notable example is given for PSRB1133+16 ($u \sim 10$), by comparing days 257 and 450 in Fig. 1(f). Even though a data-taking problem corrupted the correlation analysis of this pulsar, it is clear that on day

257 the apparent decorrelation bandwidth is 0.1 – 0.2 MHz, while on day 450 it is probably bigger than 4 MHz. We now discuss two individual pulsars which require special consideration.

5.4 PSRB2016+28

PSRB2016+28 (Fig. 3(f)) shows large variations of the parameter c_3, which according to the model (equation 16) should only vary if the velocity varies. The pulsar has an abnormally small proper motion which, combined with a distance of 1.3 kpc, leads to a transverse relative velocity of 12 ± 18 km s^{-1} in RA and 6 ± 12 km s^{-1} in declination (Lyne et al. 1982). These are of the same order as the Earth's 30 km s^{-1} orbital velocity, and so the net relative velocity varies substantially over a year. We show in Fig. 6 the variation of predicted velocity over a one-year period for 9 combinations of proper motions within the range of their error bars. The net speed varies by factors of 4 to 6 during the year, with the locations of the maxima and minima quite variable. We compared these with the measured scintillation velocity in Fig. 3(f) and found that an offset in proper motion of 1.8σ less and 1.0σ more than the nominal values gave a good match to the data; this model is indicated by the dotted line in the velocity plot of Fig. 3(f). As given by equation (C12) the predicted V_{ISS} assumes a standard of rest at the screen (i.e. the ISM). As indicated in (C16) this is also an effective pattern velocity with respect to the Earth; it has a contribution due to the 'screen' velocity as well as due to the pulsar via the 'lever arm'. In our estimate we cannot distinguish these two contributions. In our calculations we used the Sun as the standard of rest, and have not attempted to add the motion of the Sun with respect to the 'local standard of rest'. Note also that the assumed distance of 1.3 kpc enters in estimating the pulsar velocity from the proper motion. Frail & Weisberg (1990) allow a very wide range of distances (2.2 ± 1.2 kpc) for this pulsar, which adds further uncertainty to our numerical result. Thus the offset in proper motion from the nominal VLBI-measured value does not necessarily reflect a refinement of the pulsar's proper motion.

The optimum pattern velocity was also used to compute the values of s_0, shown by the dashed line in the centre right hand panel of Fig. 3(f). An alternative determination is also possible as that velocity offset which minimized the rms fluctuations of s_0. In this case the reduction in the rms values was by a factor of about 10 and gave a somewhat different velocity offset. In conclusion, it seems clear that the apparent variations of c_3, and so of time-scale, are largely due to the effect of the Earth's velocity.

5.5 PSRB1642-03

Another special pulsar is PSRB1642-03. For this pulsar, there are two widely differing estimates of the distance: 1300 pc from DM measurements and 160 pc from neutral hydrogen measurements (Manchester & Taylor 1981; Lyne et al. 1982; Frail & Weisberg 1990). The latter distance value is supported by the claim that the line of sight to the pulsar crosses a substantial HII region (Graham et al. 1974; Prentice & ter Haar 1969). Thus, for the given value of proper motion, there

are two choices for the transverse relative velocity for this pulsar. When these are used, in combination with our data for c_3, to derive a mean value for s_0, they yield values which differ by the ratio of the two distances, as listed in Table 3, under Measured Parameters. The expected values for s_0 are also listed for the two possible distances, under Predicted Parameters. Since, for a given value of v_d, these depend on distance as $\sqrt{Z}$, the two expected values for s_0 differ only by the square root of the ratio of the two distances. As can be seen, the value from the data matches the expected value better for 1300 pc than for 160 pc. For the shorter distance the measured s_0 is less than one quarter of the expected. Since the expected s_0 varies as $\sqrt{v_d}$, a smaller v_d would reduce s_0. However, the true (diffractive) v_d should be higher than the typical observed value, and hence v_d cannot be an over-estimate. Thus, it would seem that the data are more consistent with a distance of 1300 pc than 160 pc. A similar conclusion follows from a velocity comparison using Table 3; V_{ISS} agrees better with the proper motion velocity, when using 1300 pc compared with using 160 pc.

Another feature of our results for this pulsar is the fact that the obvious drift of features in the dynamic spectrum does not change sign for over 400 d. There are no changes in the sign of c_2 in Fig. 3(e), even though there are significant changes in c_1. In fact, the same sign of the drift is seen for 408-MHz dynamic spectra data of 1982 November and 1983 June for this pulsar (Hewish, Wolszczan & Graham 1985). We suggest that this indicates a stable large-scale, refractive displacement due to a line of sight that passes through the edge of an HII or other ionized region. One can even estimate the electron density needed to cause such a refraction as follows. Suppose that the line of sight passes at a distance ρ from the centre of a spherical ionized region whose electron density varies as an inverse power of ρ. The angle of refraction at wavelength λ can be written as

$$\Theta = \frac{A r_e \lambda^2 N_\rho}{2\pi} \tag{24}$$

Here N_ρ is the electron density at the point of closest approach of the line of sight to the centre, r_e is the classical electron radius and A is a constant of order unity that depends on the exponent for density versus distance. The slope in the dynamic spectra can be predicted as

$$\frac{dT}{d\nu} = \frac{1}{V}\frac{\partial X}{\partial \nu} = -\frac{2Z'(Z-Z')\Theta}{V Z f} \; ; \tag{25}$$

where Z' is the distance to the ionized region and Z is the pulsar distance. From the plots of Fig. 3(e) we take typical normalized values of c_2 as -0.07 and c_3 as 0.22 to give a slope $dT/d\nu = -c_2/2c_3 = 4.6 \times 10^{-4}$ s Hz^{-1}. Putting this value into (25) with $V = 293$ km s^{-1}, $Z = 1.3$ kpc and $Z' = 0.65$ kpc, we find a very small angle $\Theta \approx 0.05$ milliarcsec and, from equation (24), density $N_\rho \approx 1.5$ electron cm^{-3}, which is reasonable for the density in the outer part of an HII region. With this density an HII region of typical size would not contribute significantly to the dispersion measure. For the smaller pulsar distance the density $N_\rho \approx 0.18$ electron cm^{-3}. The smaller distance with the dispersion measure of 34 pc cm^{-3} implies a high average density of 0.23 cm^{-3}. Under this scenario the HII region should account for most of the dispersion measure, which would have to fill a large fraction of the line of sight, which seems unlikely. Thus this interpretation also favours the larger distance; we also note
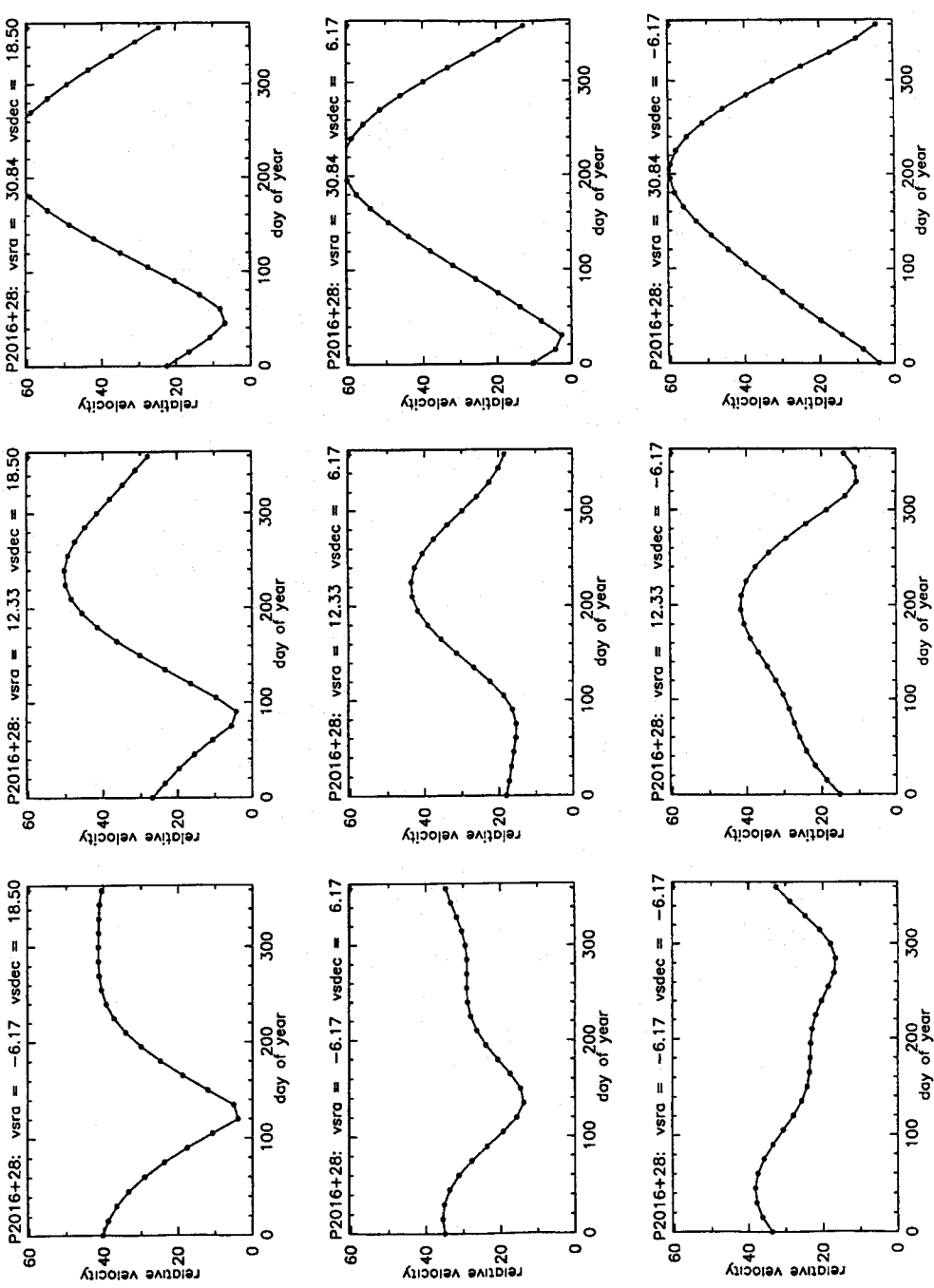
Figure 6. Predicted transverse speed of the pattern for PSRB2016+28 as a function of day of year for different values of proper motion. 'vsra' and 'vsdec' give the proper motion velocity components in RA and declination in units of km s^{-1}. The relative velocity is also in km s^{-1}. The centre panel is at the nominal proper motion as measured by Lyne et al. (1982); the top row is at a positive offset of 1.5 standard deviations in vsdec; the bottom row is at an equal negative offset in vsdec; the left column is at a negative offset of 1.5 standard deviations in vsra; the right column is at an equal positive offset in vsra; the value that fits the data $V_{\rm ISS}$ best is the middle of the left column.

that Frail & Weisberg (1990) find no convincing evidence for the nearby distance. Our interpretation is also consistent with the suggestion of Prentice & ter Haar (1971) that the line of sight to this pulsar passes through the H II region ζ Oph. Similar values are obtained for the pulsar PSRB0628-28, which also exhibits drifts in the dynamic spectra which do not change sign.

We note that Stinebring & Foster (private communication 1993) report substantial periodicities in dynamic spectra for this pulsar at frequencies of 900 and 1400 MHz. Our data do not show such phenomena, but it is possible that they are finer than our 20-kHz resolution.

6 THE EFFECT OF CURVATURE IN REFRACTIVE PHASE

In all of the foregoing, our model assumes a linear refractive phase at each epoch. In Appendix B a refractive phase model is given including the next order term (i.e. curvature) in the

Taylor expansion. The results are a modified set of equations for the three c-parameters (B3-B5) and intensity (B8). The axis orientation is no longer a free parameter and so both V_x and V_y are unknowns, as well as ϕ_x and ϕ_y and the 'gain' parameters G_x and G_y, which are determined by ϕ_{xx} and ϕ_{yy} and whose product gives the intensity. There are not enough data in the observations to determine these parameters and so we have not pursued this model in detail. It should be noted that the basis of the linear and quadratic phase shift model is a very wide separation of the diffractive and refractive scales; equivalently this requires small-amplitude refractive variations. The observed variations are sometimes as high as ±30 per cent, which strains this limit of validity, especially for u values less than about 40 (i.e. for 3 out of 6 of the pulsars studied). The model should thus be considered as a guide to the phenomena, with better quantitative agreement expected for the more heavily scattered pulsars.

The model predicts variations in c_3, which should be partially correlated with variations of intensity. Such a correlation is evident for PSRB0823+26 and to a lesser extent for

PSRB0834+06, but not for the other pulsars. For the Kolmogorov spectrum the fractional variations in G_x are approximately $R_F^2\phi_{xx}$, whose typical (rms) value can be estimated as $R_F^2[D_\phi(s_r)]^{1/2}/s_r^2$ which in turn is $\propto u^{-1/3}$. The observed intensity fluctuations are consistent with this expression, but are too sparsely sampled to test it precisely. There should also be some correlation between intensity variations and c_2. Consider a special case in which V_y is zero. Then, since c_2 depends on ϕ_x and G_x depends on ϕ_{xx}, c_2 and intensity should be correlated with an offset in time, which approximates the refractive time-scale. The physical idea here is that a positive peak in c_2 comes from a maximum tilt of the refractive wavefront; as time goes by the phase gradient decreases – that is the curvature increases, converging the waves – and so the intensity increases and at the same time the diffractive scintles are 'squeezed' together, which shortens the diffractive time-scale (c_3 increases). This is reversed for the opposite sign of a c_2 peak. Unfortunately, when V_y is also non-zero the peak correlation level will be reduced. We see no convincing sign of this phenomenon in our data. But, since the data are not sampled closely enough to follow individual refractive maxima, we cannot exclude it either. We also note that the large-scale phase curvature modulates the pattern, causing refractive amplitude variations and squeezing or stretching of the pattern, there will also be changes in the details of the diffraction pattern due to increases or decreases in the size of the effective scattering disc.

The apparent fluctuations of c_3 are explained for PSRB2016+28 as velocity variations, and for PSRB0823+26 (and possibly PSRB0834+06) as associated with refractive convergence and divergence. For PSRB2016+28, c_3 varies due to episodes of periodic modulation as discussed below. However, PSRB0329+54, PSRB0628-28 and PSRB1642-03 also show variations at the 10–20 per cent level that are marginally significant and remain unexplained in our refractive model.

7 PERIODIC MODULATIONS IN DYNAMIC SPECTRA

In our discussion so far we have only considered cases where the refractive phase fronts do not interfere before reaching the observer. As discussed above, phase curvature causes the waves either to diverge or to converge, giving refractive intensity fluctuations. In an extreme case signals could be superposed from two refractive phase fronts, corresponding to two distinct angles of arrival. Then an image-forming telescope would reveal two diffraction-broadened images of the source. In the time-frequency plane of the dynamic spectra, each refractive phase gradient produces a drift of the intensity features. Thus two images would produce two drift rates in dynamic spectra. These can be observed as criss-cross or 'V' shaped patterns. Furthermore, interference effects between the two images can produce periodic modulations of the intensity with time and frequency. Under suitable conditions these could show up as fringe patterns in the dynamic spectra, akin to the fringes produced in a double slit experiment.

Though pulsar dynamic spectra are usually dominated by a single drift rate of the diffractive scintles, multiple drift rates are also observed (e.g. Hewish 1980; Cordes et al. 1985). In addition Clegg, Fiedler & Cordes (1993) have recently reported a new phenomenon in observations of PSRB0823+26 at 1410 MHz, which often shows dual drift rates. They have found that the frequency of a local peak of intensity can sometimes shift by many MHz, over times short compared to the diffractive time-scale. Their interpretation is that the signal travels two different paths to the observer and the frequency shift is caused as one path takes over dominance of the intensity from the other. The phenomenon of periodic modulations of the diffractive patterns is also seen at some epochs. Such fringe-like patterns are seen for PSRB2016+28 in our data set (Fig. 5) and have been previously observed in other pulsars (e.g. Cordes & Wolszczan 1986; Hewish et al. 1985; Roberts & Ables 1982). We briefly consider a simple model for these effects and their implication for the power spectrum of the ISM.

7.1 Theory

Consider, first, two distinct images that dominate the angular spectrum. The conditions under which this might arise are discussed below – one scenario was outlined above. When two images with angles of arrival θ_1 and θ_2 interfere, the resulting intensity variation as a function of time and frequency can be written as (Cordes et al. 1986)

$$I(f,t) = I_1(f,t) + I_2(f,t)$$
$$+ 2[I_1(f,t)I_2(f,t)]^{1/2}\cos[\phi(f,t) + \psi(f,t)],$$
(26)

where $I_1(f,t)$ and $I_2(f,t)$ are intensity patterns due to the individual images, $\phi(f,t)$ is the geometric phase difference between the two paths (due to the different refractive phase gradients) and $\psi(f,t)$ is the diffractive phase difference associated with the images. The latter is expected to change from one scintle to the next in the dynamic spectra, while the former will change much more slowly – on the order of the refractive scale. The oscillating term in equation (20) causes the intensity modulation. The depth of this modulation depends on the relative strengths of the two images, being more prominent when the two images are of similar strengths. In the presence of other, non-interfering images, the overall background intensity level in the dynamic spectra would increase, making these modulations less prominent.

In the general two-dimensional case, the periodicities of the resulting intensity fringes in frequency and time are given by (Cordes et al. 1986)

$$P_f = \frac{2c}{3Z(\theta_2^2 - \theta_1^2)}$$
(27)

$$P_t = \frac{\lambda}{V\,|\theta_2 - \theta_1|\cos\zeta},$$
(28)

where ζ is the angle between $\theta_1 - \theta_2$ and V. In order that these periodicities be visible, at least one of them needs to be sufficiently smaller than the corresponding width in frequency or time, i.e. $P_f < 2\nu_d$, or $P_t < 2s_0/V$. The factors of 2 give the full width of typical scintles in the dynamic spectra. Also, the resolution of the observation in each domain should be smaller than the corresponding periodicity so that the oscillations are not averaged out. It is useful to express the number of fringes per diffractive scintle as

$$\frac{2\nu_d}{P_f} = \frac{6(\theta_2^2 - \theta_1^2)}{2\pi\theta_d^2}$$
(29)

$$\frac{2\tau_0}{P_t} = \frac{|\theta_2 - \theta_1|}{\pi\theta_d}, \qquad (30)$$

where $\tau_0 = s_0/V$, $\zeta = 0$ has been assumed for convenience, and equations (3) and (4) have been used for s_0 and v_d. Under the condition that both periodicities are resolved, the total number of fringes seen in a scintle (on an average) will be the larger of these two ratios. These expressions provide a useful measure for visibility of the fringe patterns in terms of the refractive and diffractive scattering angles. However, they do not address the question of what conditions might give rise to a pattern dominated by two distinct images.

One scenario for double imaging requires the overlapping of wavefronts due to larger than usual refractive shifts. The strength of the convergence due to refractive phase is characterized by $\delta G_x = R_F^2 \phi_{xx}$. This has an rms value $u^{-1/3}$ for a pure Kolmogorov spectrum. Interference requires $|\delta G_x| > 1$, which can equally be expressed as requiring refraction angles $\theta_r > \theta_d$. This condition becomes increasingly rare as u increases. At a fixed value of u, overlapping will not normally occur. When it does occur, the number of fringes in a diffractive scintle will be quite small. Only on the rare occasions that θ_1 or θ_2 exceeds its rms value by large amounts will substantial numbers of fringes be seen. If this is the mechanism, then periodic patterns should be the exception rather than the rule for pure Kolmogorov spectra, and the occurrences should become less frequent as u increases. Hewish et al. (1985) counted 3–5 fringes for PSRB1133+16 and PSRB1642–03 and so concluded $\theta_r \simeq (3–5)\theta_d$, which does not seem compatible with the Kolmogorov spectrum. In the foregoing scenario one would expect to see fringes most dramatically when the slope of the diffractive scintles changes sign, and the intensity and c_3 are both maxima due to convergence of the waves.

Goodman et al. (1987) have considered another scenario for double and multiple imaging and the associated periodic patterns. They studied the occurrence of caustics for a Kolmogorov medium with a significant inner scale cut-off. They described the signal at an observing point as the superposition of sub-images, which are analogous to rays. On occasion, sub-images can merge and make a caustic. Caustics become significant when in strong scattering the inner scale exceeds s_0. For a screen, the number of sub-images then approximates the square of the ratio of the scattering disc size to the inner scale size. For small values of the inner scale, there will thus be a large number of sub-images giving a random diffractive pattern. However, if just a few of the sub-images contribute a major fraction of the total flux at a point, interference between them will cause prominent periodic modulations. This condition becomes more likely with large values of the inner scale ($R_F \leq s_i \leq s_r$). Some of these aspects will be explored in detail in a paper in preparation, where we present results of numerical simulations of RISS effects in dynamic spectra.

7.2 Observations of periodic intensity patterns in dynamic spectra

Dual drift rates, the simplest effect of multiple imaging, are often seen for PSRB0834+06 and PSRB1919+21 (Cordes et al. 1985; Cordes & Wolszczan 1986). Our results do not show many cases with strong dual drift rates. The most obvious ones in Fig. 1 are PSRB0834+06 (day 45), PSRB1133+16 (days 0 and 257) and PSRB2016+28 (day 480). In the autocorrelation functions of dynamic spectra, dual drift rates show up as diagonal distortions or 'wings' of the lower level contours, as in Fig. 2 for PSRB0823+26 (days 1 and 16).

Periodic interference patterns have been observed in dynamic spectra for PSRB0628-28 and PSRB0834+06 (Roberts & Ables 1982); PSRB1642–03 (Hewish et al. 1985); PSRB0919+06 and PSRB1133+16 (Cordes & Wolszczan 1986). Most of these observations are at frequencies around 400 MHz. In most of these cases, the authors report only the epochs where periodic patterns are seen, but they do not indicate how often such epochs occur for a given pulsar, nor do they give quantitative estimates of the depth of periodic modulation. The visibility of such periodicities is influenced by several factors, including the number of cycles that can be resolved across a scintle and the depth of modulation of the periodicity. From our data we note that *prominent* periodic features, in which the depth of modulation is greater than about 30 per cent, are the exceptions rather than the rule. The best examples are for PSRB2016+28 on days 96 and 480. For the other pulsars mentioned above that are common to our data (PSRB0628-28, PSRB0834+06, PSRB1133+16 and PSRB1642–03), no prominent periodic fringes are seen in 10 or more epochs over 16 months. There are, however, occasional low-level periodic modulations noticeable for PSRB0823+26 and PSRB0834+06. In one case the latter pulsar exhibits very fine regular periodicity at a low level of modulation; this case is being Fourier analysed and will be the subject of a separate short paper. In addition, PSRB1133+16 often shows quasi-periodic patterns, as in Fig. 1(f); these are difficult to quantify, because the number of coherent fringes is small (2–3), so that they are not visible in a correlation analysis. In addition our data for PSRB1133+16 were corrupted by an erratic error in the data-recording.

Evidently, the Gaussian-elliptical model (or even the Shishov model) fails to produce a reasonable fit to the correlation functions under interference conditions. In our data analysis this is manifest as uncharacteristically small estimates for the parameter c_1, and a relatively large mean square error in the fit, such as for PSRB2016+28 (Fig. 3(f). A useful technique for analysing such data is to evaluate the two-dimensional Fourier Transform and scan it for significant peaks corresponding to the periodicities (Pidwerbetsky 1988). Since we have only a few cases of periodic patterns, we did not perform this analysis. Rough estimates of the refraction angles can be made for the two cases by measuring the spacing between fringes along the frequency and time lag axes in the acf of the dynamic spectra and using equations (27) to solve for θ_1 and θ_2. For PSRB2016+28 on day 96, this yields $\theta_1 = 2.4\theta_d$ and $\theta_2 = -2.1\theta_d$; for day 480 the results are $\theta_1 = 2.6\theta_d$ and $\theta_2 = -2.1\theta_d$. These calculations assume no projection effect ($\zeta = 0$) as there is no information about this. Since a projection effect would reduce the true value of P_t, the required angles would turn out be larger than those estimated above. These results imply contribution from regions of the phase screen that are as much as twice (or more) the radius of the scattering disc away from the point directly 'above' the observer. For a pure Kolmogorov spectrum the rms angle of refraction is found as in equation (20) to equal $\theta_d u^{-1/3}$, i.e. to be smaller than θ_d. A sample θ_r equal to $2\theta_d$ should thus be a very rare occurrence. The probability of such an event would be enhanced by the presence of a large inner scale – i.e. between R_F and s_r (Goodman et al. 1987). An alternative might be an increase in the

refracting power at scales near s_r. These ideas will be explored further in a paper under preparation.

8 CONCLUSIONS

We have presented a summary of the variability seen in diffractive interstellar scintillations as observed in the dynamic spectra of pulsars. The data centred on 408 MHz were recorded at Jodrell Bank from 8 pulsars at 10 or more epochs spanning a period of 480 d. We have particularly emphasized variations in the time-frequency slope and in the characteristic bandwidth and the time-scale of of the scintillation features (scintles). These were quantified by fitting an elliptical Gaussian function to the two-dimensional acf of each dynamic spectrum, and by studying the time evolution of the three fitted parameters. We have interpreted the parameter variations as the effects of refraction in the interstellar medium.

The refractive effects were analysed by separating the phase fluctuations of an equivalent thin screen into diffractive and refractive parts. Changing angles of refraction cause the diffractive pattern to be displaced laterally by an amount that is frequency and position dependent. These modulations were expressed as a modification of the two-dimensional auto-correlation function of the intensity pattern. Associated expressions were derived for the fitted parameters both for a Gaussian model for the acf, and for the 'Shishov' model. The latter is based on a more physical model of the scattering, but it did not significantly improve the modelling of individual acfs. The observed variability of the fitted Gaussian parameters was compared with the model prediction.

The drifting features are characterized by the cross-term c_2 in the Gaussian acf. This parameter varies about zero as expected for 4 out of 6 pulsars. The theoretical relative visibility of the drifting features was examined and predicted to decrease with increasing strength of scattering; however, the observed visibility parameter does not agree in detail with the prediction. For two pulsars (PSRB0628-28 and PSRB1642-03) the drifts did not change sign, which suggests the existence of a long-lived refracting structure in the line of sight. The method provides a measurement of refraction angles of 0.05 mas, which at 408 MHz would require a baseline of 450 Earth radii to resolve with VLBI techniques. For PSRB1642-03 we derived an electron density of about 1 cm^{-3}, which is consistent with current models for H II regions (ζ Oph). For the other pulsars the time-scale for changes in c_2 cannot be estimated from the data, but there is a hint that this time-scale is longer than the RISS time, which if confirmed would imply large structures in the line of sight with more refracting power than expected for a Kolmogorov medium. Such structures might or might not be a part of the suggested turbulent cascade. This possibility needs a more regularly sampled sequence of observations.

Variations and bias of the decorrelation bandwidth, caused by refractive modulation, were examined. Expressions were given for the magnitude of the bias and the rms modulation, which depend on the strength of scattering. The corrected decorrelation bandwidths derived from the data still agree fairly well with values in the literature, since the bias is not much greater than their typical uncertainties. The only notable exception is PSRB0834+06, for which the decorrelation bandwidth is greater by a factor of 8 or more. The corrected decorrelation bandwidths provide the best estimates of the

scattering strength through the simple equation (4). Observers need to be aware of how unstable the decorrelation bandwidth is, particularly for nearby objects at the higher radio frequencies.

The fitted parameter sets were also used to derive estimates for the changing refractive shifts of each pulsar. The measured values were within a factor of about two of the rms values predicted from the decorrelation bandwidth. Values for the diffractive spatial scale s_0 were also obtained. For PSRB1642-03, the estimated value favours the distance of 1.3 kpc over the alternative 160 pc, which has also been proposed. A revised formula for scintillation velocity was derived, greater by a factor of three than that of Cordes (1986). It gives reasonable agreement with proper motion estimates of pulsar velocity, where the latter is much greater than the Earth's 30 km s^{-1}. In the case of PSRB2016+28 the scintillation velocity has a pronounced annual variation. Adjustment of the pulsar velocity for the best fit gave a value within the errors of its measured proper motion. However, the undetermined velocity of the scattering medium with respect to the Sun is probably also important here.

The linear refractive phase front assumption predicts c_3 to remain constant with epoch. However, most of the observed pulsars show some variation of c_3 – i.e. of the scintillation time-scale. Three types of variation were considered. First, velocity variation for low-velocity pulsars, in which the Earth's velocity becomes significant. Only for PSRB2016+28 is this thought to be important, as discussed under scintillation velocity above. Secondly, when a curvature of the refractive phase is included, variations of c_3 are expected, which should be partially correlated with the RISS intensity fluctuations. For PSRB0823+26 this correlation is seen; however, the sampling is too coarse to make a strong statement on this or the other pulsars. The third type of variation occurs when periodic bands develop in the spectra. Prominent examples occurred on two occasions for PSRB2016+28, which had the effect of increasing c_3 (shortening the time-scale, and raising the velocity). This effect is combined with the annual velocity modulation for this pulsar. Variations of c_3 are also observed which do not fit any of the three explanations. However, their significance is somewhat marginal considering the estimation error due to the finite number of scintles.

Our models for refractive effects do not explain the periodic intensity modulation of the diffractive scintles seen in some dynamic spectra. Such interference patterns and multiple drift rates signify two or more distinct images dominating the observed image of the source. This condition should occur rather infrequently for a pure Kolmogorov spectrum and large strength of scattering, becoming more common with an increasing inner scale and/or reduced strength of scattering. Our data set has two epochs where we see pronounced periodic patterns and a number of less prominent examples; this may be consistent with a Kolmogorov spectrum with an inner scale comparable with the Fresnel scale, but a full theory of the effect is still lacking. This is in contrast with observations reported in literature, where the authors have reported periodicities to be more common and inconsistent with the Kolmogorov model. We suggest that more data need to be collected to define the statistics of such occurrences. In addition a quantitative theory (or a large-scale simulation) is needed before such statistics can be confidently interpreted in terms of the interstellar electron density spectrum.

where s_0 is the spatial decorrelation width (coherence scale) and v_d is the decorrelation bandwidth (Cordes et al. 1986; Chashei & Shishov 1976). Though the two assumptions required above are not always valid, there are some special conditions when they provide a useful approximation. In particular, the first assumption, also known as the Gaussian field approximation, is met asymptotically under conditions of strong scattering and when consideration is limited to the high-frequency part of the spatial intensity cross-spectrum (Codona et al. 1986a,b; Dashen 1979). The strong scattering condition is generally true for the ISM for frequencies less than a few GHz and path lengths larger than, say, 200 pc. Since C_d is taken as the intensity correlation under diffractive ISS conditions, it naturally corresponds to the high-frequency expansion of the intensity cross-spectrum derived by Codona et al. (1986b). Hence the second condition is also satisfied. The second assumption required for the validity of equation (A1) is harder to satisfy. For pure power-law spectra, the phase structure function varies as $s^{\beta-2}$ and is a square law only for $\beta = 4$. However, in the presence of an inner scale, the phase structure function is modified for lags smaller than the size of the inner scale to a square-law function (Coles et al. 1987). Now, if the inner scale is larger than the coherence scale, s_0, then the phase structure function will be a square law until beyond the coherence scale, which, under conditions of strong scattering, also determines the intensity decorrelation scale for the high-frequency part of the intensity spectrum. Once again, since C_d approximates the high-frequency part of the intensity spectrum, it would then be valid to use a square-law structure function for the phase fluctuations. In fact, the typical value of the inner scale proposed by Coles et al. (1987) is of the order of the Fresnel scale, which, in strong scattering conditions, is much larger than s_0.

Use of equation (A1) in equation (14) yields the following expression for C_r :

$$C_r(v, \tau) = \frac{1}{(1 + d_4 v^2)} \exp\left[-\frac{(d_1 v^2 + d_2 v\tau + d_3\tau^2)}{(1 + d_4 v^2)}\right]; \quad (A2)$$

where the parameters d_1, d_2, d_3 and d_4 are given by

$$d_1 = \frac{4(X^2 + Y^2)}{f^2 s_0^2}; \quad d_2 = \frac{4(XV_x + YV_y)}{f s_0^2}$$

$$d_3 = \frac{V_x^2 + V_y^2}{s_0^2}; \quad d_4 = \frac{1}{v_d^2}. \quad (A3)$$

Although this model has one more parameter than the Gaussian-elliptical model, in essence it is very similar to it. Whereas the parameters d_2 and d_3 are analogous to c_2 and c_3 of the Gaussian-elliptical model, the frequency decorrelation term is decoupled into a 'purely diffractive' term (d_4) and a term due to refractive effects (d_1). For values of d_4 small compared to d_1 and d_3, this model, at small lags (or, equivalently, at larger correlation levels), is very similar to the Gaussian model. At large lags (lower correlation values) the constant correlation contours taken on a 'winged' structure because of the effect of d_4. This effect, when combined with a relatively large value of d_2, can lead to a correlation function exhibiting a dual slope character.

REFERENCES

Abramowitz M., Stegun I.A., 1965, eds, Handbook of Mathematical Functions. Dover Publications, New York
Armstrong J.W., Rickett B.J., 1981, MNRAS, 194, 623
Chashei I.V., Shishov V.I., 1976, AZh, 53, 26
Clegg A.W., Fiedler R.L., Cordes J.M., 1993, ApJ, 409, 691
Codona J. L., Creamer D. B., Flatte S. M., Frehlich R. G., Henyey F. S., 1986a, J. Math. Phys., 27, 171
Codona J. L., Creamer D. B., Flatte S. M., Frehlich R. G., Henyey F. S., 1986b, Radio Sci., 21, 929
Codona J. L., Creamer D. B., Flatte S. M., Frehlich R. G., Henyey F. S., 1986c, Radio Sci., 21, 805
Cole TW., Slee O.B., 1980, Nat, 285, 93
Coles W.A., Frehlich R.G., Rickett B.J., Codona J.L., 1987, ApJ, 315, 666
Cordes J.M., 1986, ApJ, 311, 183
Cordes J.M., Wolszczan A., 1986, ApJ, 307, L27
Cordes J.M., Weisberg J.M., Boriakoff V., 1985, ApJ, 288, 221
Cordes J.M., Pidwerbetsky A., Lovelace R.V.E., 1986, ApJ, 310, 737
Dashen R., 1979, J. Math. Phys., 20, 894
Dennison B., Thomas M., Booth R.S., Brown R.S., Broderick J.J., Condon J.J., 1984, A&A, 135, 199
Ewing M.S., Batchelor R.A., Friefeld R.D., Price R.M., Staelin D.H., 1970, ApJ, 162, L169
Frail D.A., Weisberg J.M., 1990, AJ, 100, 743
Goodman J.J., Narayan R., 1985, MNRAS, 214, 519
Goodman J.J., Romani R.W., Blandford R.D., Narayan R., 1987, MNRAS, 229, 73
Graham D.A., Mebold U., Hesse K.H., Hills D.L., Wielebinski R., 1974, A&A, 37, 405
Gupta Y., Rickett B.J., Coles W.A., 1993, ApJ, 403, 183
Harrison P.A., Lyne A.G., 1993, MNRAS, 265, 778
Hewish A., 1980, MNRAS, 192, 799
Hewish A., Wolszczan A., Graham D.A., 1985, MNRAS, 213, 167
Lee L.C., Jokipii J.R., 1975, ApJ, 201, 532
Lyne A.G., Smith F.G., 1982, Nat, 298, 825
Lyne A.G., Anderson B., Salter M.J., 1982, MNRAS, 201, 503
Manchester R.N., Taylor J.H., 1981, AJ, 86, 1953
Pidwerbetsky A., 1988, PhD Thesis, Cornell University, Ithaca, NY
Prokhorov A.M., Bunkin F.V., Gochelashvily K.S., Shishov V.I., 1975, Proc. IEEE, 63, 790
Prentice A.J.R., ter Haar D., 1969, MNRAS, 146, 423
Rickett B.J., 1969, Nat, 221, 158
Rickett B.J., 1970, MNRAS, 150, 67
Rickett B.J., 1986, ApJ, 307, 564
Rickett B.J., Coles W.A., Bourgois G., 1984, A&A, 134, 390
Roberts J.A., Ables J.G., 1982, MNRAS, 201, 1119
Romani R.W., Narayan R., Blandford R.D., 1986, MNRAS, 220, 19
Scheuer P.A.G., 1968, Nat, 218, 920
Smith F.G., Wright W.C., 1985, MNRAS, 214, 97
Spangler S.R., 1988, in Cordes J.M., Rickett B.J., Backer D.C., eds, AIP Conf. Proc. No. 174, Radiowave Scattering in the Interstellar Medium. AIP, New York, p. 32
Wolszczan A., Cordes J.M., 1987, ApJ, 320, L35

APPENDIX A: THE SQUARE-LAW MODEL (SHISHOV MODEL)

Under the assumptions of (i) correlation of intensity equal to the square of the second moment of the field and (ii) a square-law structure function for the phase fluctuations, C_d can be analytically calculated as

$$C_d(\xi, \eta, v) = \frac{1}{(1 + v^2/v_d^2)} \exp\left[-\frac{(\xi^2 + \eta^2)}{s_0^2(1 + v^2/v_d^2)}\right], \quad (A1)$$

APPENDIX B: RISS EFFECTS WITH CURVED REFRACTIVE PHASE FRONT

We consider here the effects of the second-order terms in equation (9). The refractive shifts X and Y are given by equation (11). These can then be expressed in terms of the coefficients defined in equations (10a) and (10b) as

$$X(x,y) = \frac{Z}{k}[\phi_x + \phi_{xx}(x - x_0) + \phi_{xy}(y - y_0)] ; \qquad (B1)$$

$$Y(x,y) = \frac{Z}{k}[\phi_y + \phi_{yy}(y - y_0) + \phi_{xy}(x - x_0)] . \qquad (B2)$$

Note the dependence of the refractive shifts on the distance from the reference point (x_0, y_0). X depends on y and vice versa via the ϕ_{xy} term; this makes the analysis cumbersome. Thus we now choose the orientation of the axes such that $\phi_{xy} \equiv 0$.

Equations (13) and (14) are still appropriate for relating $C_\tau(v, \tau)$ to $C_d(\xi, \eta, v)$. Taking C_d to be the Gaussian form of equation (15), we find the parameters for the Gaussian model to be

$$c_1 = \frac{1}{v_d^2} + \frac{4R_F^4}{s_0^2 f^2}[\phi_x^2 G_x^4 + \phi_y^2 G_y^4] , \qquad (B3)$$

$$c_2 = \frac{4R_F^2}{s_0^2 f}[\phi_x V_x G_x^3 + \phi_y V_y G_y^3] , \qquad (B4)$$

$$c_3 = \frac{1}{s_0^2}[V_x^2 G_x^2 + V_y^2 G_y^2] , \qquad (B5)$$

where $G_x = 1/(1 + \phi_{xx}Z/k)$ and $G_y = 1/(1 + \phi_{yy}Z/k)$. Note that, unlike the linear phase front case, further simplifications by rotation of the axes are not available since this choice is exhausted by setting $\phi_{xy} = 0$.

We can also obtain an expression for the fluctuation of the average intensity at any epoch of observation, under conditions of RISS. The received electric field can be expressed in terms of the phase fluctuations imposed by the phase screen using the Fresnel integral and the intensity can be calculated from this. Splitting the screen phase into a diffractive and refractive part and using equation (9) for the refractive phase, the Fresnel diffraction integral can be rewritten as (Pidwerbetsky 1988; Cordes et al. 1986)

$$f(\mathbf{r}, Z) = \frac{G^{1/2}}{R_F'} e^{j\psi} \int_{-\infty}^{\infty} \exp[-j\phi_d(\mathbf{r}_1)] \times \exp\left[\frac{-j\pi|\mathbf{r} - \mathbf{r}_1|^2}{R_F'^2}\right] d^2\mathbf{r}_1, \qquad (B6)$$

where ψ is a constant phase factor;

$$R_F' = G^{1/2} R_F \qquad (B7)$$

is the modified Fresnel radius; and

$$G = G_x G_y = \frac{1}{(1 + \phi_{xx}Z/k)(1 + \phi_{yy}Z/k)} . \qquad (B8)$$

Equation (B8) requires $|\phi_{xx}|, |\phi_{yy}| \ll k/Z$, i.e. small intensity modulations. Here the local mean intensity for the epoch is given by G and depends on the curvature of the refractive phase. The effect of this curvature is also included in the expressions for c_1, c_2, c_3.

The special conditions of $\phi_{xx}, \phi_{yy} = 0$ correspond to $G = 1$ and yield the linear phase front results. $\phi_{xx}, \phi_{yy} < 0$ correspond to $G > 1$ and corresponding increases in the magnitudes of the three c-parameters. This is the focusing regime.

Conversely $\phi_{xx}, \phi_{yy} > 0$ correspond to $G < 1$ (the defocusing regime) where the c-parameters are reduced. Other combinations of ϕ_{xx} and ϕ_{yy} will give more complex modulations of the c-parameters. Note that the parameter c_3 is no longer independent of the refractive phase fluctuations. This could explain the observed fluctuations of c_3 for the pulsar data, over and above those due to relative velocity modulations. Some degree of correlation is expected between fluctuations of each of the c-parameters and the intensity, because of the similar nature of the dependence on the curvature term. However there will also be offset correlations between ϕ_x and ϕ_{xx} and between ϕ_y and ϕ_{yy}, which substantially complicate the parameter variations over time. Unlike the linear phase front case, there are more unknown quantities than equations in (B3)-(B5) and (B8), and it is not possible to invert them to obtain estimates of the refractive phase parameters at each epoch. Note, however, that the condition $4c_1 c_3 > c_2^2$ is still valid.

APPENDIX C: SCINTILLATION VELOCITY FOR AN ASYMMETRICALLY PLACED SCREEN

The idea of a 'scintillation speed' has been used by several observers to characterize the velocity of the Earth with respect to the DISS pattern (e.g. Rickett 1970; Lyne & Smith 1982; Cordes 1986; Harrison & Lyne 1993). In the latter two studies the scintillation speed was measured and found to be highly correlated with the proper motion speed, obtained from VLBI observations of 26 pulsars (Lyne et al. 1982). Here we give an appropriate definition of scintillation speed, assuming a single screen asymmetrically placed between source and observer. Since our result disagrees with earlier usage, we include a complete derivation.

The scintillation pattern speed is defined by

$$V_{ISS} = \frac{s_d}{\tau_d}. \qquad (C1)$$

Here τ_d is the measured characteristic time for the diffractive scintillations and s_d is the characteristic scale of the scintillation pattern at the Earth. The latter is estimated from a measurement of the characteristic decorrelation bandwidth v_d for the diffractive scintillations, and a formula suitable to the geometry of the observations. V_{ISS} estimates the apparent velocity of the pattern with respect to the observer. We follow the convention of Cordes (1986), and use v_d as the frequency offset to give an intensity correlation of 0.5, and s_d and τ_d to be the spatial and temporal widths at a correlation of 1/e, all measured at a centre frequency of f. Note that in the following f is formally the geometric mean of the two observing frequencies in the correlation analysis, and λ is the corresponding free-space wavelength. f will be negligibly different from the arithmetic mean in typical observations.

We need a theoretical expression for the intensity correlation versus spatial offset and frequency offset. We need to include motion of the pulsar, the Earth and the medium. Ideally we would do the calculation for a point source and a screen geometry and also for an extended scattering medium. A complete solution to the latter problem does not exist and we proceed with the screen problem. A point source (pulsar) is a distance L_p from a scattering screen; it is viewed by an observer a distance L_o from the screen. We start with the simpler problem of a plane wave incident on a thin screen at a distance L from an observer. The field phasor at the observer

is given by the Fresnel diffraction integral (e.g. equation (5) of Cordes et al. 1986); the intensity at a single point is given by the squared magnitude of the phasor. This depends only on properties of the screen and the Fresnel scale $R_F = \sqrt{\lambda L/2\pi}$. The result is then correct for the point source (pulsar) geometry, if the screen parameters are unchanged and the length L is replaced by $L_{eff} = L_p L_o/(L_p + L_o)$.

In very strong scattering it has been shown that the correlation of diffractive intensity fluctuations $\rho(b, v, f)$ versus frequency offset v and spatial offset b can be approximated by

$$\rho(b, v, f) = |\Gamma_d(b, v, f)|^2. \quad (C2)$$

Here Γ_d is a second moment of the field, modified to remove the effect of the group delay which fluctuates over very large scales; this is sometimes referred to as a refractive effect (equation 26 in Lee & Jokipii 1975). These authors consider Γ_d in both an extended medium and a screen limit. We do not use their extended medium result since it corresponds to a plane wave incident on a thick layer, rather than a point source in the scattering medium. The scattering of a plane wave incident on a thin screen can be characterized by its structure function for phase at centre frequency f:

$$D_\phi(b) = <[\phi(b') - \phi(b' + b)]^2>. \quad (C3)$$

If the phase screen has a two-dimensional spectrum $\propto$ wavenumber$^{2+\alpha}$,

$$D_\phi(b) = (b/s_0)^\alpha \quad (C4)$$

where s_0 defines the characteristic scale for the screen. In (C4) the special case $\alpha = 2$ is easy to solve, giving

$$\rho(b, v, f) = \frac{1}{1+w^2} \exp\left[\frac{-b^2}{s_0^2(1+w^2)}\right] \quad (C5)$$

where

$$w = \frac{v}{f} \frac{R_F^2}{s_0^2}. \quad (C6)$$

The widths s_d and v_d, defined above, become

$$s_d = s_0 \quad (C7)$$

$$v_d = f s_0^2/R_F^2. \quad (C8)$$

When these are put into equation (C1) we obtain

$$V_{ISS} = \frac{\sqrt{L c v_d / 2\pi}}{\tau_d f} \quad (C9)$$

where c is the speed of light.

Now we turn to the pulsar geometry, in which $x = L_o/L_p$ and L_T is the observer to pulsar distance. In (C8) we only need to replace L by L_{eff} in R_F, which gives

$$L_{eff} = L_T x/(1+x)^2. \quad (C10)$$

However, the apparent temporal scale is not quite so easy since it involves motion of the observer (V_o) with respect to the screen and motion of the pulsar (V_p) with respect to the screen (using the screen as the reference frame). This situation can be analysed using the method of appendix B of Rickett (1986) or by using a 'lever arm argument'. In decorrelation time τ_d the pulsar moves vector displacement $V_p \tau_d$, while the observer moves $V_o \tau_d$. The straight line through these displaced positions intercepts the screen at offset r_{eff}; a decorrelation to $1/e$ occurs when r_{eff} equals s_0, i.e.

$$V_p \tau_d (L_o/L_T) + V_o \tau_d (L_p/L_T) = s_0 \quad (C11)$$

which gives

$$|x V_p + V_o| = V_{ISS} = (1+x)s_0/\tau_d, \quad (C12)$$

which defines V_{ISS} for the pulsar geometry. An alternative derivation of the second equality in (C12) involves the use of (C1) and noting that the scale at the observer is given by $s_d = s_0(1 + x)$. Now we put (C10) into (C8), and solve for s_0 in terms of L_T, x and v_d and substitute into (C12). Hence we find

$$V_{ISS} = \frac{\sqrt{L_T c x v_d / 2\pi}}{\tau_d f}. \quad (C13)$$

Putting this into practical astronomical units:

$$V_{ISS} = 3.85 \times 10^4 \frac{\sqrt{v_{d,MHz} L_{kpc} x}}{f_{GHz} \tau_{d,s}} \, km\, s^{-1}. \quad (C14)$$

For a mid-placed screen, $x=1$ and (C12) shows that V_{ISS} estimates the vector *sum* of pulsar and observer velocities with respect to the screen. We use (C14) with $x=1$ in analysing our data; however, we note that it is a factor 3 greater than equation (6) of Cordes (1986). In that paper the details of the derivation are not given; we note that the derivation depends critically on the precise definitions of v_d and τ_d. We also note that the formula used by Lyne & Smith (1982) is about twice that of Cordes and so only 0.7 times our equation (C14).

Another way of thinking is to consider the motion of the diffraction pattern relative to the observer. The 'lever arm' causes the pattern to move in the opposite direction to the pulsar, which accounts for the sum in (C11). A screen close to the pulsar ($x > 1$) magnifies the effect of V_p and vice versa. For velocities with respect to an arbitrary reference frame, the relation (C12) becomes

$$V_{ISS} = |x V_p' + V_o' - (1+x) V_{screen}'| = |V_{patt}' - V_o'|. \quad (C15)$$

Using the lever arm method we find that the pattern velocity relative to the *observer* is

$$V_{patt} = |-x V_{p,o} + (1+x) V_{screen,o}|. \quad (C16)$$

Using the observer's reference frame, (C15) gives the same result for V_{ISS}. Evidently our definition of V_{ISS} is the same as the pattern velocity.

Equation (C13) was derived for particular conditions, which may not apply in the ISM. We used the special case of $\alpha = 2$; a more reasonable assumption is $\alpha = 5/3$. The correction necessary in (C13) is to reduce the multiplier by only 2 per cent. This is negligible in comparison to the other uncertainties. The value $x=1$ is a simple but unjustified choice; the correction for an extended scattering medium has yet to be determined, even when stationary; the superposition of differing scattering layers with differing velocities seems quite likely and so generates a further uncertainty. Equation (C2) applies only in asymptotic strong scattering. Codona et al. (1986c) have shown how it should be modified for intermediate scattering strength; the modification is small in typical DISS observations.

APPENDIX D: CHARACTERIZATION OF THE SLOPES AND THEIR INFLUENCE ON THE DISS BANDWIDTH

In equation (22) we define p as a visibility index for the sloping features in dynamic spectra. We now apply the model of equation (16) and hence estimate an average value for p as a function of u the strength of scattering.

$$p = \frac{c_2^2}{4c_1c_3} = \frac{X^2}{X^2 + Y^2 + s_0^2 f^2/(4\nu_d^2)}. \tag{D1}$$

Using equation (4) we rewrite $s_0^2 f^2/\nu_d^2$ as s_r^2, which using equation (20) becomes $<X^2> u^{2/3}$, and hence

$$<p> = \left\langle \frac{X^2}{X^2 + Y^2 + <X^2> u^{2/3}/4} \right\rangle. \tag{D2}$$

Taking $<X^2> = <Y^2>$, and making the crude approximation that the average of the ratio of random variables is the ratio of their means, we find

$$<p> \sim \frac{0.5}{1 + u^{2/3}/8}. \tag{D3}$$

A first-order correction to this shows that it overestimates $<p>$ by at most 25 per cent and that it correctly displays the dependence on u.

A similar analysis can be used to study the variability of the apparent decorrelation bandwidth $\nu_{d,app} = 1/\sqrt{c_1}$. Equation (16) gives

$$c_1 = \frac{4(X^2 + Y^2)}{f^2 s_0^2} + \frac{1}{\nu_d^2} = \frac{(1 + R/g)}{\nu_d^2}, \tag{D4}$$

where $R = (X^2 + Y^2)/<X^2 + Y^2>$ is a random variable with an exponential distribution with unit mean, and $g = u^{2/3}/8$. Hence

$$\frac{\nu_{d,app}}{\nu_d} = \frac{1}{\sqrt{1 + R/g}}. \tag{D5}$$

Since R has a simple probability density we can determine both the mean and variance of $\frac{\nu_{d,app}}{\nu_d}$.

$$\frac{<\nu_{d,app}>}{\nu_d} = \sqrt{\pi g} \exp(g) \operatorname{erfc}(\sqrt{g}) \tag{D6}$$

and

$$\frac{<\nu_{d,app}^2>}{\nu_d^2} = g \exp(g) \operatorname{E}_1(g). \tag{D7}$$

In the foregoing expressions, erfc is the complementary error function and E_1 is the exponential integral as defined by Abramowitz & Stegun (1965). These expressions are used to derive the plots of Fig. 5, which display the mean and the modulation index of $\nu_{d,app}/\nu_d$ as a function of u. This analysis gives a quantitative form to the idea that isolated estimates of the decorrelation bandwidth are biased and variable due to the influence of the refractive shifts.